

Note: This work has not yet been peer-reviewed and is provided by the contributing author(s) via EarthArXiv.org as a means to ensure timely dissemination of scholarly and technical work on a noncommercial basis. Copyright and all rights therein are maintained by the author(s) or by other copyright owners. It is understood that all persons copying this information will adhere to the terms and constraints invoked by each author's copyright. This work may not be reposted without explicit permission of the copyright owner.

This work is under review at the *Journal of Physical Oceanography*. Copyright in this work may be transferred without further notice.

2 **Dynamics of eddying abyssal mixing layers over rough topography**

3 Henri F. Drake\*

4 *Princeton University / Geophysical Fluid Dynamics Laboratory, Princeton, New Jersey,*  
5 *United States*

6 *Previously, MIT–WHOI Joint Program in Oceanography/Applied Ocean Science &*  
7 *Engineering, Cambridge and Woods Hole, Massachusetts, United States.*

8 Xiaozhou Ruan and Raffaele Ferrari

9 *Massachusetts Institute of Technology, Cambridge, Massachusetts, United States*

10 Jörn Callies

11 *California Institute of Technology, Pasadena, California, United States*

12 Kelly Ogden

13 *Western University, London, Ontario, Canada*

14 Andreas M. Thurnherr

15 *Lamont-Doherty Earth Observatory, Palisades, New York, United States*

16 \* *Corresponding author:* Henri F. Drake, [henrifdrake@gmail.com](mailto:henrifdrake@gmail.com)

## ABSTRACT

17 The abyssal overturning circulation is thought to be primarily driven by small-scale tur-  
18 bulent mixing. Diagnosed watermass transformations are dominated by rough topography  
19 “hotspots”, where the bottom-enhancement of mixing causes the diffusive buoyancy flux  
20 to diverge, driving widespread downwelling in the interior—only to be overwhelmed by an  
21 even stronger upwelling in a thin Bottom Boundary Layer (BBL). These watermass trans-  
22 formations are significantly underestimated by one-dimensional sloping boundary layer so-  
23 lutions, suggesting the importance of three-dimensional physics. Here, we use a hierarchy  
24 of models to generalize this one-dimensional boundary layer approach to three-dimensional  
25 eddying flows over realistically rough topography. When applied to the Mid-Atlantic Ridge  
26 in the Brazil Basin, the idealized simulation results are roughly consistent with available  
27 observations. Integral buoyancy budgets isolate the physical processes that contribute to  
28 realistically strong BBL upwelling. The downwards diffusion of buoyancy is primarily bal-  
29 anced by upwelling along the canyon flanks and the surrounding abyssal hills. These flows  
30 are strengthened by the restratifying effects of submesoscale baroclinic eddies on the canyon  
31 flanks and by the blocking of along-ridge thermal wind within the canyon. Major topo-  
32 graphic sills block along-thalweg flows from restratifying the canyon trough, resulting in the  
33 continual erosion of the trough’s stratification. We propose simple modifications to the one-  
34 dimensional boundary layer model which approximate each of these three-dimensional ef-  
35 fects. These results provide *local* dynamical insights into mixing-driven abyssal overturning,  
36 but a complete theory will also require the *non-local* coupling to the basin-scale circulation.

## 37 1. Introduction

38 Below the oceanic pycnocline, the vast volumes of the deep ocean are ventilated by two  
39 interconnected cells of a global meridional overturning circulation (Gordon 1986). The  
40 lower cell of this circulation is sourced along the coast of Antarctica, where atmospheric  
41 cooling and brine rejection transform surface waters into the dense Antarctic Bottom Waters  
42 (AABW) that fill the global abyssal ocean at a rate of approximately 30 Sv ( $1 \text{ Sv} \equiv 10^6 \text{ m}^3/\text{s}$ )  
43 (Talley 2013). Since the buoyancy surface bounding AABW from above does not outcrop  
44 elsewhere in the ocean, conservation of mass implies that in steady state an equal amount  
45 of AABW must upwell across buoyancy surfaces (diabatically) from the abyss. Waters  
46 below about 2000 m depth (corresponding to the crests of major topographic features, such  
47 as mid-ocean ridges) can upwell diabatically only in the presence of interior watermass  
48 transformations (e.g. small-scale turbulent mixing) or fluxes across the seafloor boundary  
49 (geothermal heating) (Munk 1966; Walin 1982; Tziperman 1986; Ferrari 2014).

50 These basic inferences of a global diabatic upwelling from the abyss (e.g. Sverdrup et al.  
51 1942) are also consistent with more detailed inverse modelling at regional scales (e.g. Talley  
52 et al. 2003). Most notably, Hogg et al. (1982) consider the fate of 4 Sv of AABW (colder  
53 than  $0^\circ\text{C}$ ) that enters the Brazil Basin from the Southern Ocean through the Vema Channel;  
54 since there are no other exits from the basin and since geothermal fluxes are relatively weak,  
55 they infer that turbulent mixing must diffuse heat downward at a rate of  $\mathcal{O}(3 \text{ cm}^2/\text{s})$  to  
56 balance the upwelling of these waters across the  $0^\circ\text{C}$  isotherm.

57 Early in-situ turbulence measurements in the upper  $\sim 1000$  m of the interior ocean sug-  
58 gested turbulent diffusivities more than an order of magnitude smaller than those predicted  
59 by the large-scale abyssal tracer budgets described above (Gregg 1987; Ledwell et al. 1993).

60 A subsequent celebrated field campaign in the abyssal waters of the Brazil Basin reported  
61 similarly weak background diffusivities over the smooth topography of the abyssal plains,  
62 but revealed diffusivities that increased downwards by several orders of magnitude over the  
63 rough topography of the Mid-Atlantic Ridge (Polzin et al. 1997; Ledwell et al. 2000). Using  
64 regional inverse and forward approaches, respectively, St. Laurent et al. (2001) and Huang  
65 and Jin (2002) modelled the impacts of the observed bottom-enhanced mixing on the re-  
66 gional circulation: bottom-enhanced mixing drove interior downwelling while upwelling was  
67 restricted to a thin layer of buoyancy convergence near the bottom boundary (as opposed  
68 to Munk 1966’s uniform upwelling model) and the basin-scale horizontal circulation was  
69 dominated by narrow mixing-driven flows along ridge flanks (as opposed to the interior  
70 geostrophic flow predicted by Stommel 1958).

71 The development of mixing parameterizations (e.g. St. Laurent and Garrett 2002; Kunze  
72 et al. 2006; Polzin 2009; Melet et al. 2014; de Lavergne et al. 2020) allowed these Brazil  
73 Basin results to be generalized to global abyssal watermass transformations (e.g. Nikurashin  
74 and Ferrari 2013; de Lavergne et al. 2016; Kunze 2017; Cimoli et al. 2019). Based on such  
75 estimates, Ferrari et al. (2016) and McDougall and Ferrari (2017) revised the conceptual  
76 model of the global mixing-driven abyssal upwelling: mixing-driven diabatic upwelling is  
77 confined to a thin Bottom Boundary Layer (BBL) just above the insulated (or geothermally  
78 heated) seafloor, while bottom-enhanced mixing drives diabatic downwelling in the Stratified  
79 Mixing Layer (SML) above; the net diabatic overturning is the small remainder of these  
80 two large opposing mixing layer flows. In this emerging framework, the global overturning  
81 circulation is modulated by the dynamics of thin BBLs (Callies and Ferrari 2018; Drake et al.  
82 2020). Since these abyssal boundary layer flows are challenging to observe (Naveira Garabato  
83 et al. 2019; Spingys et al. 2021) and are too thin to be resolved by conventional general

84 circulation models, however, they remain poorly understood (Drake 2021 and Polzin and  
85 McDougall 2022 discuss outstanding questions).

86 The interpretation of the role of boundary mixing in the abyssal overturning circulation  
87 (dating back to Munk 1966) has a contentious history: on the one hand, in-situ observa-  
88 tions of weakly-stratified bottom mixed layers seemed to imply the existence of vigorous  
89 boundary mixing (Armi 1978); on the other hand, it was argued that mixing of already  
90 well-mixed waters was inefficient and thus did not lead to significant watermass transforma-  
91 tion (see Garrett’s 1979 comment and Armi’s 1979b reply). Garrett (1990) later formalized  
92 his criticism using sloping boundary layer theory (Phillips 1970; Wunsch 1970) and sug-  
93 gested that one-dimensional flows up the sloping bottom boundary—driven by the mixing  
94 itself—could provide sufficient restratification to resolve this conundrum. Based on obser-  
95 vations of homogeneous layers detached from the bottom boundary (but carrying distinct  
96 levels of suspended sediments), Armi (1978, 1979a) instead proposed a three-dimensional  
97 boundary–interior exchange process whereby layers are rapidly mixed when they impinge  
98 upon topographic features (e.g. seamounts or abyssal hills) and are eventually restratified  
99 by along-isopycnal exchanges with the stratified interior.

100 In light of recent diagnostic evidence for boundary-control on the abyssal circulation (Fer-  
101 rari et al. 2016), Callies (2018) revisited these ideas to test whether sloping BBL theory is  
102 quantitatively consistent with observations. In his analysis of the sloping flank of the Mid-  
103 Atlantic Ridge in the Brazil Basin (where co-located measurements of both abyssal mixing  
104 rates and stratification are available), he found that the steady state 1D boundary layer so-  
105 lution forced by the observed mixing exhibits a stratification an order of magnitude weaker  
106 than observed. The watermass transformations sustained by 1D dynamics alone (Garrett

107 1990) are thus too inefficient to contribute significantly to the global abyssal overturning  
108 circulation.

109 To reconcile boundary layer dynamics with observations, Callies (2018) argued the strat-  
110 ification of abyssal mixing layers may be maintained by submesoscale baroclinic eddies,  
111 which act to slump sloping buoyancy surfaces back to the horizontal. Mixing-driven 1D  
112 boundary layer solutions are linearly unstable to submesoscale baroclinic modes (Wenegrat  
113 et al. 2018; Callies 2018), in a manner similar to the well-studied analagous problem in  
114 the surface mixed layer (Boccaletti et al. 2007; Fox-Kemper et al. 2008). Callies (2018)  
115 simulated the finite amplitude evolution of these instabilities in a 3D generalization of the  
116 1D boundary layer framework and showed that the solutions converge on a substantially  
117 stronger quasi-equilibrium stratification that is more consistent with observations.

118 As acknowledged by Callies (2018), however, it is not clear to what extent such idealized so-  
119 lutions are directly applicable to the mid-ocean ridge, which is characterized by particularly  
120 rough topography. For example, many of the observations of bottom-enhanced mixing, strat-  
121 ification, and diabatic upwelling from the region are confined to  $\mathcal{O}(500\text{ m})$ -deep fracture zone  
122 canyons which cut across the ridge (Polzin et al. 1997; Ledwell et al. 2000; St. Laurent et al.  
123 2001; Thurnherr and Speer 2003). To account for these leading-order topographic features,  
124 Ruan and Callies (2020) ran simulations of mixing-driven flow over a sinusoidal mid-ocean  
125 ridge incised by an idealized Gaussian fracture zone canyon. They confirm Thurnherr and  
126 Speer’s (2003) speculation that the canyon sidewalls suppress cross-canyon (or along-slope)  
127 flow and thus support a vigorous up-canyon (or cross-slope) mean flow. The restratifying  
128 tendency of this up-canyon mean flow is much stronger than that of either the 1D up-slope  
129 flow or the submesoscale eddies on the smooth ridge flanks, implying that abyssal water-  
130 mass transformations are, per unit area, four times larger within the canyons than on the

131 ridge flanks. Ruan and Callies (2020) found, however, that the simulated stratification in  
132 the canyon is orders of magnitude larger than observed, suggesting their simulations are  
133 still missing important physics. In addition to fracture zone canyons, mid-ocean ridges are  
134 also characterized by smaller-scale anisotropic abyssal hills; these features have character-  
135 istic scales taller than 1D BBLs and comparable to those of the fastest growing baroclinic  
136 mode (Callies 2018; Wenegrat et al. 2018), so we would expect them to affect both mean  
137 and eddying circulations. Within the fracture zone canyons, abyssal hills often manifest  
138 as sills that substantially block or constrain the deep up-slope flow (Thurnherr et al. 2005;  
139 Dell 2013; Dell and Pratt 2015); hydraulic acceleration over the sill produces relatively large  
140 velocities also associated with locally enhanced turbulence (Clément et al. 2017).

141 Here, we use a hierarchy of analytical and numerical solutions to bridge the gap between  
142 idealized 1D BBLs and the complexity of observed flows in a region scarred by a fracture  
143 zone canyon and dotted with abyssal hills. In Section 2, we review key insights from the  
144 1D BBL buoyancy budget and derive a generalized buoyancy budget that permits topo-  
145 graphic variations and spatio-temporal eddy correlations. In Section 3, we describe the  
146 “slope-aligned” simulation configuration which leverages a coordinate frame aligned with  
147 the mean topographic slope to allow restratification by mean up-slope flow across a uniform  
148 background vertical buoyancy gradient. In Section 4, we describe the simulated mixing  
149 layer flows in a simulation with realistic topography and show they are qualitatively con-  
150 sistent with available observations. In Section 5, we present simulated buoyancy budgets,  
151 and show a balance between bottom-enhanced mixing, submesoscale eddy fluxes, and the  
152 cross-slope mean flow. By progressively simplifying the configuration in a hierarchy of mod-  
153 els framework (Held 2005), we isolate the roles of individual physical processes in setting  
154 the near-boundary stratification. In Section 6, we discuss how our results bridge the gap

155 between interpretations of in-situ observations (e.g. Armi 1978; Thurnherr and Speer 2003;  
 156 Thurnherr et al. 2020) and 1D BBL theory (e.g. Garrett 1979; Garrett et al. 1993), and  
 157 how they illustrate—at a regional scale—the control of abyssal mixing layers on an “upside-  
 158 down” abyssal overturning circulation (Ferrari et al. 2016). We conclude that a combination  
 159 of mixing-driven up-slope flows, submesoscale baroclinic eddies, and topographic control  
 160 are required to maintain a steady state near-boundary stratification consistent with in-situ  
 161 observations and a finite global abyssal overturning circulation.

## 162 **2. Theory**

163 We review the derivation and results of sloping boundary layer theory in Sections 2a,b in  
 164 anticipation of our generalization to three-dimensional flows over rough sloping topography  
 165 in Section 2c.

### 166 *a. Slope-aligned equations*

167 In sloping boundary layer theory (Wunsch 1970; Phillips 1970; Garrett et al. 1993; Thomp-  
 168 son and Johnson 1996; Callies 2018; Holmes and McDougall 2020), analytical progress is  
 169 achieved by modelling the system in a coordinate frame aligned with its mean topographic  
 170 slope, rather than the typical coordinate frame  $(\hat{x}, \hat{y}, \hat{z})$  with  $\hat{z}$  aligned with gravity. It is  
 171 useful to decompose the buoyancy  $B = N^2 \hat{z} + b$  into a background component  $N^2 \hat{z}$ , where  
 172  $N^2$  is a constant vertical buoyancy gradient, and a perturbation component  $b(\hat{x}, \hat{y}, \hat{z}, t)$ ; the  
 173 background buoyancy is assumed to be in hydrostatic balance with a background pressure  
 174 and we similarly decompose  $P = \frac{1}{2} N^2 \hat{z}^2 + p$ . Then, we rotate the coordinate system to a  
 175 coordinate frame aligned with the mean-slope  $(x, y, z) \equiv (\hat{x} \cos \theta + \hat{z} \sin \theta, \hat{y}, \hat{z} \cos \theta - \hat{x} \sin \theta)$ ,  
 176 where  $\theta$  is the region’s average slope angle in the  $\hat{x}$ -direction (e.g. dashed black lines in Fig-

177 ure 3b). For small slopes<sup>1</sup>  $\tan \theta \ll 1$ , the hydrostatic Boussinesq equations in the mean-slope  
 178 coordinates are, at leading order, given by

$$u_t + \mathbf{u} \cdot \nabla u - fv \cos \theta = -p_x + b \sin \theta + \nabla \cdot (\nu \nabla u), \quad (1)$$

$$v_t + \mathbf{u} \cdot \nabla v + fu \cos \theta = -p_y + \nabla \cdot (\nu \nabla v), \quad (2)$$

$$p_z = b \cos \theta, \quad (3)$$

$$\nabla \cdot \mathbf{u} = 0, \quad (4)$$

$$b_t + \mathbf{u} \cdot \nabla b + N^2(w \cos \theta + u \sin \theta) = \nabla \cdot [\kappa (N^2 \cos \theta \mathbf{z} + \nabla b)], \quad (5)$$

179 where subscripts represent partial derivatives,  $\nabla$  is the gradient operator,  $u$  is the along-  
 180 canyon (or cross-slope) velocity,  $v$  is the cross-canyon (or along-slope) velocity,  $w$  is the  
 181 slope-normal velocity,  $f$  is a constant Coriolis parameter,  $\kappa$  is an isotropic eddy diffusivity,  
 182 and  $\nu = \sigma \kappa$  is an isotropic eddy viscosity determined by the turbulent Prandtl number  
 183  $\sigma$ . The rotated along-canyon  $\mathbf{x}$ -momentum equation is identical in form to the zonal  $\hat{\mathbf{x}}$ -  
 184 momentum equation with the exception of the small but dynamically significant projection  
 185 of the perturbation buoyancy force  $b\hat{\mathbf{z}}$  on  $\mathbf{x}$ .

186 The anomalous seafloor depth, relative to the mean slope, is given by

$$d(x, y) = \hat{d}(\hat{x}, \hat{y}) + \hat{x} \tan \theta \quad (6)$$

187 We set  $z = 0$  along the sloping plane that intersects the point with the greatest anomalous  
 188 seafloor depth,  $\max(d)$  (see Figure 2). Boundary conditions at the seafloor,  $z = \max(d) -$

---

<sup>1</sup>While  $\sin \theta \simeq \theta$  and  $\cos \theta \simeq 1$  in this limit, we retain these geometric terms explicitly so they are not forgotten.

189  $d(x, y)$ , are  $\mathbf{u} = 0$  (no-slip<sup>2</sup> and no-normal-flow) and  $\mathbf{n} \cdot (\kappa \nabla B) = 0$  (insulating<sup>3</sup>), where  $\mathbf{n}$   
 190 is a unit vector normal to the boundary.

191 *b. Smooth planar slopes and steady 1D dynamics*

192 Assuming a constant topographic slope ( $d \equiv 0$ ) and mixing rates that vary only in the  
 193 slope-normal direction, the equilibrium solution reduces to

$$-fv \cos \theta = b \sin \theta + \partial_z (\nu u_z), \quad (7)$$

$$fu \cos \theta = \partial_z (\nu v_z), \quad (8)$$

$$p_z = b \cos \theta, \quad (9)$$

$$uN^2 \sin \theta = \partial_z [\kappa (N^2 \cos \theta + b_z)], \quad (10)$$

194 where the continuity equation  $w_z = 0$  combines with the no-normal-flow bottom boundary  
 195 condition at  $z = 0$  to require  $w \equiv 0$  everywhere (no slope-normal exchange). These equa-  
 196 tions can be solved analytically in the case of constant parameter values (Wunsch 1970;  
 197 Phillips 1970; Thorpe 1987; Garrett 1990), or approximately for varying parameters in some  
 198 asymptotic limits (Salmun et al. 1991; Callies 2018). In either case, the slope Burger number  
 199  $S \equiv N^2 \tan^2 \theta / f^2$  and the BBL thickness

$$\delta \equiv q^{-1} = \sqrt{\frac{2\nu}{f}} (1 + S\sigma)^{-\frac{1}{4}}, \quad (11)$$

200 emerge as key parameters. We recognize  $\delta$  as the Ekman layer thickness  $\delta_E \equiv \sqrt{\frac{2\nu}{f}}$ , modified  
 201 by buoyancy effects at the sloping boundary; for typical abyssal values,  $S \ll 1$  and  $\sigma = \mathcal{O}(1)$   
 202 such that buoyancy effects are weak (Thurnherr and Speer 2003).

---

<sup>2</sup>While applying a bottom drag to match the unresolved Reynolds' stresses in the turbulent log-layer would be a more defensible option (Taylor and Shaw 1920), we choose the no-slip condition for a closer correspondence to 1D BBL models.

<sup>3</sup>Geothermal heating is thought to contribute negligibly to abyssal watermass transformations in the BBTR canyon region (Thurnherr et al. 2020), so we ignore it for simplicity here.

203 Recalling the crucial assumption of a constant background vertical stratification  $N^2$ , the  
 204 slope-aligned buoyancy equation (10) describes a direct balance between slope-normal diffu-  
 205 sion of heat downwards towards the boundary and cross-slope advection against the constant  
 206 background buoyancy gradient; this balance is a near-boundary analog of Munk's (1966)  
 207 classic interior ocean vertical balance. This is best illustrated by integrating (10) in the  
 208 slope-normal direction,

$$\psi(z) \equiv \int_0^z u \, dz = \kappa \cot \theta (B_z/N^2 \cos \theta) = \kappa \cot \theta (1 + b_z/N^2 \cos \theta), \quad (12)$$

209 where  $\psi$  is the up-slope transport (per along-slope unit length) and we have invoked the  
 210 insulating bottom boundary condition on the full stratification,  $B_z = 0$  at  $z = 0$ .

211 Consider the case of exponentially bottom-enhanced mixing,  $\kappa(z) = \kappa_{\text{BG}} + \kappa_{\text{BOT}} e^{-z/h}$  with  
 212  $\kappa_{\text{BOT}}/\kappa_{\text{BG}} \gg 1$ . Equation (12) reveals two keys insights:

213 1. The net up-slope transport, integrated over both the upwelling BBL and the down-  
 214 welling SML, converges to the negligibly small value<sup>4</sup>

$$\psi_\infty \equiv \psi(z \rightarrow \infty) = \kappa_{\text{BG}} \cot \theta \quad (\text{the 1D integral constraint}) \quad (13)$$

215 since far from the boundary  $b_z \rightarrow 0$  (Thorpe 1987) and both  $\kappa(z) \rightarrow \kappa_{\text{BG}}$  and  $\cot \theta$  are  
 216 small.

217 2. Maximal up-slope transport in the BBL is achieved when both  $\kappa$  is large (i.e. near the  
 218 boundary) and  $B_z$  is large (strong restratification). If the stratification is maintained  
 219 near the background value  $N^2 \cos \theta$  where the diffusivity is large (i.e.  $z \ll h$ ) then  
 220 the up-slope transport in the BBL reaches an upper bound  $\max\{\psi\} \simeq \kappa_{\text{BOT}} \cot \theta =$   
 221  $\frac{\kappa_{\text{BOT}}}{\kappa_{\text{BG}}} \psi_\infty \gg \psi_\infty$ .

---

<sup>4</sup>While  $\psi_\infty \rightarrow \infty$  as  $\theta \rightarrow 0$ , the adjustment timescales also grows,  $\tau_{\text{BBL}} = \delta^2/\kappa_{\text{BG}} \propto \cot \theta \rightarrow \infty$ , making it more likely that other dynamics disrupt the approach to equilibrium.

222 Callies (2018) derives approximate but analytical boundary layer solutions to the steady  
 223 1D system (eqs. 7–10) for bottom-enhanced mixing. In the abyssal ocean regime with typical  
 224 values of  $S\sigma \ll 1$ , the equilibrium stratification  $B_z$  is approximately inversely proportional  
 225 to  $\kappa$  in the SML (their eq. 10; Figure 1a, solid lines), such that the diffusive buoyancy flux  
 226  $\kappa B_z \simeq \kappa_{\text{BG}} N^2 \cos \theta$  is constant and finite buoyancy flux convergence occurs only within the  
 227 thin BBL. Since the BBL stratification is reduced to roughly  $B_z \approx \frac{\kappa_{\text{BG}}}{\kappa_{\text{BOT}}} N^2 \cos \theta$  (Figure 1a,  
 228 solid lines) and near-boundary mixing is thus inefficient, up-slope BBL transport is roughly  
 229 equal to the negligibly small integral constraint (13),  $\max\{\psi\} \simeq \kappa_{\text{BG}} \cot \theta$  (Figure 8a, dotted  
 230 and dashed lines). This weak BBL upwelling and negligible SML downwelling contrasts with  
 231 the strong bi-directional flows inferred from watermass transformation analyses (Ferrari et al.  
 232 2016; McDougall and Ferrari 2017).

### 233 *c. Rough topography and eddy fluxes*

234 We now derive the 3D BBL buoyancy budget, which allows for topographic and flow  
 235 variations along the plane of the slope. Consider the buoyancy budget for a volume  $\mathcal{V}$   
 236 within a height  $z$  above the mean slope (Figure 2):

$$\iiint_{\mathcal{V}(z' < z)} b_t \, dV = \iint_{\mathcal{A} \equiv \partial\mathcal{V}(z' < z)} (-\mathbf{u}B + \kappa \nabla B) \cdot \mathbf{n} \, dA, \quad (14)$$

237 where we use the divergence theorem to rewrite the right-hand side terms in terms of  
 238 fluxes normal to the bounding surface  $\partial\mathcal{V}$  (Figure 2). Fluxes through the seafloor at  
 239  $z' = \max(d) - d(x, y)$  vanish due to the no-flow and insulating bottom boundary condi-  
 240 tions. Motivated by the simulations in Section 3, we assume fluxes through cross-slope and  
 241 along-slope boundaries cancel due to periodicity (e.g.  $b(x) = b(x + L_x)$ ), except for the

242 up-slope flow across the background buoyancy gradient (recall  $B = N^2\hat{z} + b$ ),

$$\iint_{\mathcal{A}(x+L_x; z' \leq z)} (-uB) \, dydz' - \iint_{\mathcal{A}(x; z' \leq z)} (-uB) \, dydz' = -N^2L_x \sin \theta \iint_{\mathcal{A}(x; z' \leq z)} u \, dydz' \quad (15)$$

243 This, combined with the slope-normal component of the flux through the  $z' = z$  surface,

244 gives

$$\underbrace{\iiint_{\mathcal{V}(z' \leq z)} b_t \, dV}_{\text{LHS}} = \underbrace{-\langle -\kappa B_z \rangle}_{\text{Mixing}} \underbrace{-\langle wb \rangle}_{\text{Eddies}} \underbrace{-N^2L_x \sin \theta \Psi}_{\text{Mean Flow}}, \quad (16)$$

RHS

245 where we define  $\langle \phi \rangle \equiv \iint_{\mathcal{A}(z)} \phi \, dx dy$  as the slope-integral operation and  $\Psi(z) \equiv$

246  $\iint_{\mathcal{A}(x; z' \leq z)} u \, dydz'$  as the up-slope transport across the periodic boundary (Figure 2a). At

247 equilibrium, the form of the generalized volume-integral buoyancy equation (16) is simi-

248 lar to the 1D transport equation (12), although there is now an additional eddy flux of

249 buoyancy towards or away from the boundary, and the turbulent buoyancy flux may be

250 modified by along- and cross-slope correlations between  $\kappa$  and  $B_z$ . Assuming a steady state

251 and integrating up far into the interior, where  $\kappa \rightarrow \kappa_{\text{BG}}$  and the perturbations vanish, we

252 recover the integral constraint (13) on the net up-slope transport from the 1D solution,

$$253 \Psi_\infty / L_y = \kappa_{\text{BG}} \cot \theta.$$

254 Callies (2018) proposes a simple parameterization of restratification by 3D submesoscale

255 baroclinic eddies as a way to account for these missing physics in the 1D boundary layer

256 solution. The main effect of baroclinic eddies is to extract available potential energy from

257 the mean flow by slumping sloping buoyancy surfaces back towards the horizontal, thereby

258 maintaining a realistically-large near-bottom stratification; this adiabatic process is most

259 conventionally parameterized as an eddy overturning circulation (Gent and McWilliams

260 1990; Fox-Kemper et al. 2008). Taking advantage of thermal wind balance ( $fv_z = b_x$ ), the

261 slumping of isopycnals by baroclinic instability—which decreases horizontal buoyancy gra-  
 262 dients  $b_{\hat{x}}$ —can equivalently be parameterized as a reduction in the vertical shear  $v_z$ , e.g. by  
 263 enhanced vertical momentum diffusion (Rhines and Young 1982; Greatbatch and Lamb 1990;  
 264 Young 2011). We provide a derivation of this closure in the Appendix, in which we apply  
 265 Andrews and McIntyre’s (1976) Transformed Eulerian Mean and Gent and McWilliams’s  
 266 (1990)’s baroclinic eddy parameterization scheme to the slope-aligned framework.

267 Following Callies (2018), we thus parameterize submesoscale eddy restratification by arti-  
 268 ficially increasing the vertical eddy viscosity  $\nu = \sigma\kappa$ . Unlike Callies (2018), who simply tune  
 269  $\sigma = 230$  to match the mean behavior of their 3D model, however, we: 1) only enhance the  
 270 viscosity  $\nu_v = \sigma_v\kappa$  acting on the along-slope thermal wind (as in Holmes et al. 2019) since  
 271 the available potential energy that fuels the instabilities is stored in cross-slope buoyancy  
 272 gradients; 2) we allow the eddy viscosity to have vertical structure,  $\sigma_v = \sigma_v(z)$ , and 3) we  
 273 estimate the magnitude and structure of  $\sigma_v(z)$  from the eddy fluxes resolved by a 3D model  
 274 (Figure 1b; see Appendix). We refer to  $\Psi + \frac{\langle wb \rangle}{N^2 \sin \theta L_x}$  as the cross-slope *residual* transport  
 275 (analogous to that of the Southern Ocean, e.g. Marshall and Radko 2003), since the eddy  
 276 flux term is equal to the eddy overturning streamfunction in the limit of stationary and  
 277 adiabatic eddies, which is applicable outside of the thin BBL (Figure 11c; see Appendix).

278 Applying this simple closure to the 1D model results in weakening of the slope-normal  
 279 shear of the along-slope flow and, because of the approximate thermal wind balance  $fv_z \simeq$   
 280  $b_z \sin \theta$  that holds in the SML (eq. 8), results in a corresponding weakening of the negative  
 281 perturbation stratification  $b_z$  (equivalent to a strengthening of the total stratification  $B_z$ ;  
 282 compare dash-dotted and solid lines in Figure 1a). In this context, the 1D model’s up-slope  
 283 transport  $\psi$  is re-interpreted as the residual transport, since it also includes the eddy-induced  
 284 overturning. At equilibrium, this parameterized eddy restratification triples  $B_z$  and thus also

285  $\kappa B_z$  and the residual flow  $\psi$  at the top of the 1D solution’s BBL (Figure 1a and Figure 8a,b),  
286 bringing the watermass transformations of the 1D BBL more in line with the basin-scale  
287 overturning (Morris et al. 2001; Callies 2018).

### 288 3. Numerical model setup

289 We simulate 3D mixing-driven flows using the hydrostatic Boussinesq equations in the  
290 MIT General Circulation Model (MITgcm; Marshall et al. 1997). For simplicity, we assume a  
291 linear equation of state; because temperature units are more intuitive, we use temperature  $T$   
292 and buoyancy  $b \equiv g\alpha T$  interchangeably throughout, where  $g = 9.81 \text{ m/s}^2$  is the gravitational  
293 acceleration and  $\alpha = 2 \times 10^{-4} \text{ }^\circ\text{C}^{-1}$  is a constant thermal expansion coefficient.

#### 294 a. Realistic bathymetry

295 Most of the results describe a core realistic-bathymetry simulation of the Brazil Basin sub-  
296 region sampled by both the Brazil Basin Tracer Release Experiment (BBTRE, Ledwell et al.  
297 2000) and Dynamics of the Mid-Ocean Ridge Experiment (DoMORE, Clément et al. 2017),  
298 located on the western flank of the Mid-Atlantic Ridge. We extract the Brazil Basin’s  
299 seafloor topography from the Global Bathymetry and Topography at 15 Arc Sec dataset  
300 (SRTM15+; Tozer et al. 2019), which includes many more multibeam measurements than  
301 previous products (e.g. Smith and Sandwell 1997) and thus better resolves both the BBTRE  
302 fracture zone canyon at  $21^\circ 30' \text{ S}$  and the smaller-scale abyssal hills characteristic of mid-  
303 ocean ridges (Figure 3a). We interpolate the bathymetry onto a locally tangent Cartesian  
304 grid  $(\hat{x}, \hat{y}, \hat{z})$  aligned with the BBTRE canyon, where  $\hat{x}$  denotes the along-canyon dimension  
305 and  $\hat{y}$  denotes the cross-canyon dimension (Figure 3a), and produce a gridded bathymetry  
306 field  $\hat{d}(\hat{x}, \hat{y})$ . The simulated canyon stretches from a few km west of the Tracer Release

307 Experiment site around 18.5°W (Ledwell et al. 2000) to a few km east of the DoMORE sill  
308 that dramatically constrains the up-canyon flow at 14.5°W (Clément et al. 2017).

309 *b. Implementing the perturbation Boussinesq equations in the mean-slope coordinate frame*

310 Following Section 2a, we solve equations (1–5) in a coordinate frame aligned with the  
311 domain’s mean slope. Equations (1–5) are solved in terms of the perturbation variables,  
312 with the background buoyancy field  $N^2\hat{z}$  entering only indirectly via linear and inhomogeneous  
313 terms in the perturbation buoyancy equation, implemented as additional explicit  
314 tendency terms in the MITgcm. To stabilize the numerical solution without damping sub-  
315 mesoscale eddies, we additionally implement horizontal (in the rotated frame) biharmonic  
316 hyper-diffusion of momentum and buoyancy which acts only at scales close to the grid res-  
317 olution. Horizontal hyper-diffusive tendencies vanish in the budgets presented here, so we  
318 omit them in all of our analyses. We enforce an insulating boundary condition on the full  
319 buoyancy at the seafloor:  $\mathbf{n} \cdot (\kappa \nabla B) = 0$ .

320 Relative to the mean slope, the anomalous seafloor topography  $d(x, y) \equiv \hat{d}(\hat{x}, \hat{y}) - \hat{x} \tan \theta$  is  
321 nearly continuous across the periodic boundaries in the along-canyon direction  $\mathbf{x}$  and in the  
322 cross-canyon direction  $\mathbf{y}$ ; however, to eliminate any remaining discontinuities across these  
323 boundaries, we join the two boundaries smoothly by linear interpolation in both  $\mathbf{x}$  and  $\mathbf{y}$ .

324 By 1) removing the uniformly-stratified background state from the prognostic variables,  
325 2) formulating the model in the slope coordinate frame, and 3) making the boundary condi-  
326 tions and forcing terms periodic in the  $(x, y)$  plane, we are free to apply periodic boundary  
327 conditions to the perturbation state variables  $u$ ,  $v$ ,  $b$ , and  $p$  in both  $\mathbf{x}$  and  $\mathbf{y}$ .

328 *c. Forcing by observation-inspired bottom-enhanced turbulent mixing*

329 Following the classic one-dimensional boundary layer configuration (Wunsch 1970), we pa-  
330 rameterize small-scale turbulent mixing as a slope-normal<sup>5</sup> diffusive buoyancy flux  $-\kappa \partial_z B \mathbf{z}$ .  
331 We use Callies’ (2018) self-similar height-above-bottom profile

$$\kappa(x, y, z) = \kappa(z; d) = \kappa_{\text{BG}} + \kappa_{\text{BOT}} \exp\left(-\frac{z+d}{h}\right), \quad (17)$$

332 with  $\kappa_{\text{BOT}} = 1.8 \times 10^{-3} \text{ m}^2/\text{s}$ ,  $\kappa_{\text{BG}} = 5.3 \times 10^{-5} \text{ m}^2/\text{s}$ , and  $h = 230 \text{ m}$ ; these parameter  
333 values are chosen by performing a least-squares fit to the height-above-bottom-average of  
334 126 microstructure profiles in the BBTRE region. The sparsity and noisiness of individual  
335 mixing profiles, and disagreements in the literature about where mixing is strongest (Polzin  
336 et al. 1997; St. Laurent et al. 2001; Polzin 2009; Clément et al. 2017; Thurnherr et al. 2020),  
337 prohibit the formulation of a robust parameterization with a richer spatial structure. We  
338 imagine this imposed bottom-enhanced mixing to represent a variety of turbulent ocean  
339 processes (see Thorpe 2005), especially the breaking of internal waves (Whalen et al. 2020)  
340 but also including unspecified boundary mixing processes (Armi 1978; Armi and D’Asaro  
341 1980; Polzin et al. 2021).

342 *d. Numerics*

343 The horizontal grid spacing of  $\Delta x = \Delta y = 600 \text{ m}$  is fine enough to permit the anticipated  
344 submesoscale baroclinic turbulence, which for the 1D sloping BBL problem has a maxi-  
345 mum linear growth rate near the local deformation radius  $L \sim \frac{NH_{\text{ML}}}{f} = 6 \text{ km}$  (Stone 1966;  
346 Wenegrat et al. 2018), where  $H_{\text{ML}} \approx 250 \text{ m}$  is the thickness of the weakly-stratified bottom  
347 layer (Callies 2018). Yet, the grid spacing is also coarse enough for a three-dimensional

---

<sup>5</sup>Vertical buoyancy gradients are generally much larger than horizontal gradients, so, assuming an isotropic diffusivity, the vertical (or, for small slopes  $\theta \ll 1$ , approximately slope-normal) components of the diffusive buoyancy flux dominate.

348 simulation of the entire 480 km by 60 km region to be computationally feasible. We set  
 349 the hyper-diffusivities  $\kappa_4 \equiv \nu_4 = 2 \times 10^4 \text{ m}^4/\text{s}$ , the smallest value that maintains a stable  
 350 solution, so that hyper-diffusion interferes minimally with diapycnal buoyancy fluxes and  
 351 the growth of submesoscale instabilities (Callies 2018; Ruan and Callies 2020). In the ver-  
 352 tical, a cell thickness of  $\Delta z = 6 \text{ m}$  (with partial cells down to 1.2 m) marginally resolves  
 353 the predicted  $\mathcal{O}(10 \text{ m})$ -thick BBL. A high-resolution 1D spin-up experiment confirmed this  
 354 vertical resolution is sufficient to accurately reproduce all features of the analytical solution  
 355 (using Burns et al.’s 2016 Dedalus package; not shown). Starting at about 1000 m above  
 356 the mean slope, the cell thickness  $\Delta z$  is increasingly stretched (up to  $\Delta z = 50 \text{ m}$  at the top  
 357 of the domain) to efficiently fit both the  $h \log(\kappa_{\text{BOT}}/\kappa_{\text{BG}}) \approx 1300 \text{ m}$  vertical scale of abyssal  
 358 mixing layers (Callies 2018) and the  $\mathcal{O}(800 \text{ m})$  topography into a domain that spans a height  
 359  $H = 2700 \text{ m}$  above the mean slope.

### 360 *e. Parameter regime*

361 Following Callies (2018), we assume a background far-field stratification  $N =$   
 362  $1.3 \times 10^{-3} \text{ s}^{-1}$  and a local Coriolis parameter  $f = -5.3 \times 10^{-5} \text{ s}^{-1}$  characteristic of the  
 363 BBTRE region. Applying a linear fit to the bathymetry  $\hat{d}(\hat{x}, \hat{y})$  yields the domain’s av-  
 364 erage topographic slope angle  $\theta = 1.26 \times 10^{-3}$  in  $\hat{\mathbf{x}}$ . We assume that small-scale turbulent  
 365 mixing acts similarly to mix buoyancy and momentum, i.e. we assume a turbulent Prandtl  
 366 number of  $\sigma \equiv \frac{\nu}{\kappa} = 1$ . Because we resolve submesoscale instabilities, we do not need to  
 367 parameterize their restratification by increasing  $\sigma$ . Mixing layers are thus characterized by  
 368 weak stratification and gentle large-scale slopes, equating to a small slope Burger number,  
 369  $S \equiv N^2 \tan^2 \theta / f^2 = 10^{-3} \ll 1$  and BBL thickness  $\delta \approx 8 \text{ m}$  (eq. 11).

370 We spin up the simulations from a uniformly-stratified rest state ( $b = 0, p = 0, \mathbf{u} = \mathbf{0}$ ). The  
 371 BBL adjusts rapidly on a timescale  $\tau_{\text{BBL}} = \delta^2/\kappa_{\text{BOT}} = 10$  hours. While the full equilibration  
 372 of the solution occurs over a prohibitively long diffusive timescale characteristic of the abyssal  
 373 ocean interior,  $\tau_{\text{INT}} = H^2/\kappa_{\text{BG}} \approx 5000$  years, buoyancy tendencies are small enough by  
 374  $t = 13$  years in the bottom 1000 m (see Section 5) that we consider the solution sufficiently  
 375 equilibrated for the analyses presented here.

376 *f. Hierarchy of progressively idealized simulations*

377 The simulations in our model hierarchy differ only in their seafloor topography, domain  
 378 length, and dimensionality. We progressively idealize the BBTRE canyon configuration  
 379 (Figure 3f): first, we remove the abyssal hills along the ridge flank and idealize the geometry  
 380 of the remaining canyon and sill features (“Canyon+Sill”; Figure 3e); second, we remove  
 381 the sill (“Canyon”; 3d); third, we remove the canyon entirely (“Smooth3D”; Figure 3c);  
 382 and finally, we eliminate variations along the plane of the slope, collapsing the solution  
 383 onto a single slope-normal dimension as in classical BBL theory (“1D”). For reference, we  
 384 also include some additional variants on the 1D model where we vary one parameter at  
 385 a time: non-rotating (“1D $_{f=0}$ ”), non-sloping (“1D $_{\theta=0}$ ”), and parameterized submesoscale  
 386 eddies (“1D $_{\sigma_v(z)}$ ”; see Appendix). Unless we specify otherwise, results refer to the realistic-  
 387 topography BBTRE simulation.

388 **4. Mixing-driven up-canyon flow, submesoscale turbulence, and stratification**

389 At quasi-equilibrium, the time-mean flow (averaged over days 5000 to 5500) is dominated  
 390 by a vigorous up-canyon jet along the canyon thalweg, banked along the steeper southern  
 391 flank of the canyon (as in Dell 2013; Ruan and Callies 2020). The up-canyon jet exhibits a

392 maximum along-canyon-averaged velocity of  $\bar{u}^x = 0.75$  cm/s about 400 m above the seafloor  
 393 (Figure 4a). This up-slope jet is non-uniform and partially compensated by a down-slope  
 394 jet on the gentler northern flank, such that the maximum cross-canyon-averaged up-canyon  
 395 velocity is reduced to  $\bar{u}^y = \mathcal{O}(0.1$  cm/s) (Figure 4a,b). The up-slope jet accelerates as it  
 396 spills over two major cross-canyon sills: the BBTRE sill at  $x = 110$  km and the DoMORE sill  
 397 at  $x = 420$  km (Figure 4a,b); this acceleration and the spilling over of isopycnals at both sills  
 398 is suggestive of hydraulic control<sup>6</sup> (Pratt and Whitehead 2008). The vertically-integrated  
 399 cross-slope transport  $\int_{z=0}^H u dz$  is dominated by standing eddy features above the canyon  
 400 (Figure 4c, recall  $z = 0$  at the deepest point relative to the mean slope), but prominently  
 401 features meandering up- and down-canyon jets when integration is restricted to just the  
 402 canyon itself,  $\int_{z=0}^{800\text{m}} u dz$  (Figure 4d). These simulated mixing-driven means flows can be  
 403 compared against two in-situ mooring observations: the BBTRE mooring at  $x = 110$  km,  
 404 several km upstream of the BBTRE sill (Toole 2007; also analyzed by Thurnherr et al.  
 405 2005), and a DoMORE mooring at  $x = 420$  km, atop the DoMORE sill (Clément et al.  
 406 2017). At the DoMORE sill, horizontal and vertical constrictions accelerate the simulated  
 407 up-canyon flow to 5 cm/s over a layer  $\delta z = 150$  m thick and  $\delta x = 2.5$  km wide (Figure 5a).  
 408 The resulting velocities are roughly constant in time, also suggestive of hydraulic control  
 409 (Pratt and Whitehead 2008), and are about 25% those measured by the mooring (half as  
 410 fast and half as thick; Figure 5b). By contrast, the simulated up-canyon flow at the BBTRE  
 411 mooring is much weaker ( $u \approx 0.75$  cm/s) but spread over a thicker ( $\delta z \approx 600$  m) and wider  
 412 ( $\delta x \approx 5$  km) layer, such that the total up-canyon transports at the two sections are similar  
 413 (Figure 5c). It is impossible to compare against observed *transports* because single mooring  
 414 velocity profiles (e.g. Thurnherr et al. 2005) cannot be reliably extrapolated across the

---

<sup>6</sup>The DoMORE control section is evident from the canyon hydrography, but the BBTRE one is not (Thurnherr et al. 2005).

415 canyon, although such errors may be smaller at constrictions considerably narrower than  
416 the local deformation radius (Thurnherr 2000), as at the DoMORE sill. The simulated flow  
417 at the BBTRE mooring has roughly the same vertical structure as in the moored current  
418 meter velocities, but about half their magnitude (Figure 5d). The relative weakness of the  
419 simulated flows suggest that either the imposed microstructure-based mixing rates are biased  
420 low (as suggested by Thurnherr et al. 2005 and Clément et al. 2017, and by the in prep.  
421 tracer analysis by Ledwell and modelling by Odgen et al.) or that the simulation fails to  
422 capture important physics.

423 Averaging the BBTRE simulation in height-above-bottom (hab) coordinates reveals that  
424 the stratification generally remains close to its background value, except in the  $\mathcal{O}(10\text{ m})$ -  
425 thick BBL (Figure 6a, solid blue line). Upon first inspection, this result appears inconsistent  
426 with observations in the canyon which, when averaged in hab, exhibit much weaker stratifi-  
427 cation up to 600 m above the seafloor (Figure 6, dashed and dotted red lines). Most of this  
428 discrepancy is resolved by sampling the simulation at the exact locations of the observational  
429 profiles (Figure 6b), and comparing their sample mean to that of the observations (Figure 6a,  
430 red lines). Since the BBTRE sampling strategy was to find as much tracer as possible, the  
431 field campaign specifically focused on sampling the deep depressions in the BBTRE canyon,  
432 which appear to exhibit unusually weak stratification compared to the canyon flanks, sills,  
433 and the surrounding ridge flanks. However, several microstructure profiles from the 1996  
434 cruise are available along the canyon crests—just north of the domain—and on average  
435 exhibit similarly strong near-bottom stratification as in the simulation’s domain average  
436 (Figure 6a, dashed blue line). This conditional averaging exercise clarifies the significant  
437 disagreements in reported estimates of the BBTRE region’s average stratification (Polzin  
438 et al. 1997; St. Laurent et al. 2001; Polzin 2009). But even accounting for sampling bias,

439 the simulated canyon is more stratified by about a factor of two relative to the observations  
440 (see Section 6).

441 The time-mean view of the up-canyon circulation above filters out a rich field of subme-  
442 soscale eddies which have radii comparable to the deformation radius and are trapped within  
443 a few hundred meters of the seafloor, including within the  $\mathcal{O}(10\text{ km})$ -wide canyon (Figure 7).  
444 These eddies manifest themselves as spatial and temporal meanders of the mean up-canyon  
445 jet, which in the following section we show contribute significantly to the simulation’s buoy-  
446 ancy budget and to maintaining its strong near-bottom stratification.

## 447 5. Buoyancy budgets: mixing, mean flow, and eddies

448 In this section, we use a hierarchy of models to elucidate the complicated dynamics that  
449 support the up-canyon mean flows described in the previous section. Volume-integrated  
450 buoyancy budgets (eq. 16) provide the major insights and are presented in Figure 8 for each  
451 model in the hierarchy. We further separate the contributions from time-independent stand-  
452 ing eddies and transient eddies. All of the solutions exhibit substantial residual tendencies  
453 several hundred meters above the topography; however, within a few hundred meters of the  
454 ridge flanks and within the canyons, tendencies are an order of magnitude smaller than other  
455 terms in the budgets because the dynamics (vigorous mixing and submesoscale processes)  
456 within the bottom few hundred meters are much faster than the weak diffusion in the inte-  
457 rior (Figure 8, black). The 1D and  $1D_{\sigma_v(z)}$  simulations are computationally inexpensive, so  
458 we also provide their fully equilibrated solutions for context (Figure 8a,b; dotted).

459 In the classical 1D solution, a weak up-slope transport in the BBL (Figure 8a, blue line)  
460 maintains a weak near-boundary stratification, although it is already much stronger than  
461 in the flat-bottom after 5000 days of spin-up (Figure 9a). The evolution of the Smooth3D

462 solution follows the 1D solution closely until about 800 days, at which point the laminar  
463 solution becomes unstable to submesoscale baroclinic modes which rapidly grow and equi-  
464 librate at finite amplitude (Callies 2018; Wenegrat et al. 2018). At quasi-equilibrium, these  
465 transient eddies advect denser waters from the SML back into the BBL (Figure 8b, orange),  
466 effectively restratifying the BBL (Figure 9b) and thus strengthening the maximum diffu-  
467 sive buoyancy flux (Figure 8b, red). It is helpful to interpret the combination of the mean  
468 flow and the eddy fluxes as the residual circulation that advects tracers (Ferrari and Plumb  
469 2003; see Appendix). In this framing, the slope-normal eddy flux nearly doubles the resid-  
470 ual upwelling in the BBL (Figure 8b,a, green lines). The crude eddy parameterization in  
471  $1D_{\sigma_v(z)}$  qualitatively captures this restratifying effect (Figure 9b, compare dash-dotted and  
472 blue against solid grey) and enhances the residual BBL upwelling by a factor of 2–3 relative  
473 to the 1D model, both transiently and at equilibrium (Figure 8b,c; solid and dotted green  
474 lines, respectively). A more rigorous approach to parameterization is beyond the scope of  
475 this paper.

476 The volume-integrated buoyancy budget is more complicated to interpret in the presence  
477 of variable topography. In the Canyon solution, a substantial diffusive buoyancy flux con-  
478 vergence drives a vigorous up-slope mean flow within the bottom 200 m along the narrow  
479 trough of the canyon, producing a transport of 5 mSv (Figure 8d, blue) which is already  
480 larger than the total BBL transport in the 1D model (Figure 8a, blue). This strong mean  
481 flow maintains a stratification near the large background value within the canyon trough  
482 (Figures 10b; 9c, orange line). Thurnherr and Speer (2003) hypothesizes this efficient re-  
483 stratification is due to the canyon sidewalls blocking the along-slope thermal wind, such that  
484 the momentum is redirected into the cross-slope flow. The Canyon simulation’s excellent  
485 agreement with the  $1D_{f=0}$  model, in which rotation is turned off and thus the along-slope

486 thermal wind is suppressed by construction, supports their hypothesis (Figure 9c; orange  
 487 and dotted lines). Ruan and Callies (2020) hypothesize that flow across the steep canyon  
 488 flanks with  $S = \mathcal{O}(1)$  also contributes significantly to the strong stratification in the canyon.  
 489 However, this hypothesis does not explain the strong stratification along the canyon thal-  
 490 weg, where the cross-canyon slope goes to zero and local dynamics cannot sustain a finite  
 491 stratification at equilibrium in the absence of an along-canyon topographic slope.

492 The turbulent buoyancy flux also converges around a Height Above the Mean Slope  
 493 (HAMS) of  $z = 800$  m, driving an additional residual upwelling of about 13 mSv from  
 494  $z = 600$  m to 800 m dominated by the BBLs on the upper canyon flanks and on the smooth  
 495 ridge flank surrounding the canyon (Figure 8d, green line). The upwelling along the smooth  
 496 ridge flank of the Canyon simulation is about twice as large as that of the Smooth3D  
 497 simulation, despite covering a smaller area, because along-slope buoyancy gradients above  
 498 the canyon flanks provide an additional energy source for submesoscale instabilities (Fig-  
 499 ure 10d), driving an isopycnal thickness flux between the canyon and surrounding flanks  
 500 and thus maintaining a much larger stratification on the flanks (Figures 9b). In the Canyon  
 501 simulation’s quasi-equilibrium state, much of the turbulent buoyancy flux divergence in the  
 502 upper SML (far above the seafloor) is not yet equilibrated: the bottom-enhanced diffusion  
 503 of buoyancy towards the boundary slowly cools the interior (Figure 8d, red and black lines;  
 504 MacCready and Rhines (1991)).

505 In the Canyon+Sill simulation, the sill blocks up-slope flow within the trough of the canyon  
 506 (Figure 8e, d). This is expected, since the up-canyon flows of  $\mathcal{O}(1$  cm/s) only carry sufficient  
 507 kinetic energy to lift a parcel across a stratification of  $N \sim \mathcal{O}(10^{-4} - 10^{-3} \text{ s}^{-1})$  by a height  
 508  $\delta_{\text{Fr}} = U/N \sim 20 - 200$  m (based on a topographic Froude number of  $\text{Fr} \equiv N\delta_{\text{Fr}}/U \sim 2$ ),  
 509 much smaller than the sill height of  $h_{\text{sill}} = 800$  m and resulting in a blocked flow layer of

510 thickness  $h_{\text{sill}} - \delta_{\text{Fr}}$  (Baines 1979; Winters and Armi 2012), both up- and down-stream of the  
511 sill (recall the cross-slope periodicity). No up-slope mean flow is available to restratify the  
512 trough of the canyon, so it slowly homogenizes due to mixing (Figure 10c; as in Dell 2013).  
513 In contrast, within a slope-normal displacement  $\delta_{\text{Fr}}$  of the sill, mean flows along the upper  
514 parts of the two canyon flanks are able to maintain a layer of strong stratification<sup>7</sup> (Figures  
515 8e, 10e,f).

516 The structure of the stratification in the BBTRE simulation is qualitatively similar to  
517 that of the Canyon+Sill simulation, although the rougher abyssal hill topography acts to  
518 thicken the layer of enhanced stratification near the DoMORE sill height and supports a large  
519 near-bottom stratification on the hilly ridge flanks surrounding the canyon (Figure 10g,h,  
520 9b). The slope-normal structure of the BBTRE canyon’s buoyancy budgets (Figure 8f) is  
521 remarkably similar to that of the Canyon+Sill simulation and can thus be explained as the  
522 combination of the processes described—only slightly blurred in the slope-normal direction  
523 by the additional topographic roughness.

## 524 6. Conclusions and Discussion

525 By generalizing the methods of classical 1D sloping Bottom Boundary Layer (BBL) theory  
526 (Garrett et al. 1993), we construct a hierarchy of mixing-driven flow simulations that bridge  
527 the gap between three-dimensional (Armi 1978) and one-dimensional (Garrett 1979) concep-  
528 tual models of abyssal mixing layer restratification. Our choice to parameterize small-scale  
529 turbulence as a bottom-enhanced turbulent diffusivity—inspired by local microstructure  
530 measurements—considerably simplifies the analysis but may not adequately represent the

---

<sup>7</sup>Tidal velocities, omitted for simplicity here, would imply a larger excursion height, a thinner blocked flow layer, and the potential for restratification processes to penetrate deeper into the canyon trough (as hypothesized by Clément et al. 2017).

531 underlying small-scale physics (see Polzin and McDougall 2022). Nevertheless, in this con-  
532 ventional prescribed-diffusivity framework we demonstrate that the homogenizing tendency  
533 due to bottom-enhanced small-scale mixing is balanced by the restratifying effects of the  
534 residual overturning circulation, which is a combination of mean and submesoscale eddy  
535 flows (eq. 16). At equilibrium, the slow interior diffusion of heat into the abyss is balanced  
536 by a weak net upwelling (eq. 13), the result of substantial cancellation of up- and down-slope  
537 flows.

538 The simulations’ steady states are never achieved here due to the prohibitively slow dif-  
539 fusive adjustment in the interior (MacCready and Rhines 1991); in more realistic contexts,  
540 cross-slope pressure gradients due to coupling with the non-local circulation would sup-  
541 port a much more rapid adjustment process (Peterson and Callies 2021). Despite the  
542 non-equilibrated nature of our solutions, the slope-aligned framework permits simplified  
543 buoyancy budgets which facilitate our dynamical interpretation and the derivation of an  
544 eddy closure (see Appendix). Another advantage of the slope-aligned framework is that the  
545 solutions are less ambiguous than previous approaches, which either require ad hoc sponge  
546 layers at distant horizontal boundaries (Dell 2013) or can only be analyzed transiently be-  
547 fore mixing completely homogenizes buoyancy (Ruan and Callies 2020). The slope-aligned  
548 framework also permits a consistent exploration of ever more realistic configurations: from  
549 a constant topographic slope—well described by 1D BBL models (Garrett et al. 1993)—  
550 to the complex geometry of the region surrounding the BBTRE canyon. While the local  
551 nature of the sloping BBL framework is conceptually convenient for all of the above rea-  
552 sons, several important non-local factors have been ignored. For example, the inclusion of  
553 cross-slope pressure gradients (Peterson and Callies 2021) or large-scale boundary currents  
554 (MacCready and Rhines 1991; Naveira Garabato et al. 2019) would fundamentally alter the

555 transient spin-up problem. The periodic nature of the simulation may also overemphasize  
556 topographic blocking effects since upstream topographic sills also re-appear downstream.

557 The results of our quasi-realistic simulation of the Brazil Basin Tracer Release Experiment  
558 (BBTRE) reconciles two dominant boundary mixing paradigms: yes, bottom-enhanced mix-  
559 ing drives a restratifying up-slope flow in the BBL (Garrett 1979, 1990); but, this flow is  
560 much stronger than predicted by 1D theory due to net restratification by transient baro-  
561 clinic eddies and topographic steering/blocking (Armi 1978, 1979a; Thurnherr and Speer  
562 2003; Callies 2018; Ruan and Callies 2020). The net restratifying effect can to a large extent  
563 be attributed to three distinct physical restratification/destratification processes:

- 564 1. slumping of isopycnals by finite-amplitude submesoscale baroclinic instabilities (Wene-  
565 grat et al. 2018; Callies 2018),
- 566 2. the blocking of cross-canyon thermal winds within narrow fracture zone canyons (Thurn-  
567 herr and Speer 2003; Dell 2013; Ruan and Callies 2020), and
- 568 3. the effect of sills in blocking up-canyon mean flows and homogenizing depressions well  
569 below the sill height (Baines 1979; Winters and Armi 2012; Dell 2013).

570 We propose a simple parameterization for the restratifying effects of submesoscale baroclinic  
571 eddies in terms of a vertically-varying enhancement of vertical momentum diffusion (see  
572 Appendix). The blocking of along-slope flow by canyon walls can be captured in the 1D  
573 model by inhibiting the development of along-slope thermal wind, such as by setting  $f = 0$ .

574 Applied to the BBTRE model, the slope-averaged buoyancy budget (16) confirms Thurn-  
575 herr et al.’s (2020) hypothesis that spatial averaging reconciles the thin *local* BBL trans-  
576 formations implied by vertical microstructure profiles and 1D models (e.g. Thompson and  
577 Johnson 1996) with the thicker *bulk* BBL transformations implied by a decreasing topo-

578 graphic perimeter—or mixing area—with depth (Polzin 2009; Kunze et al. 2012; Holmes  
579 et al. 2018): water below the canyon crest upwells in the net, while water above downwells  
580 (Figure 16f). The spatial heterogeneity of the simulated up-canyon flow (Figures 5,6) may  
581 explain why the buoyancy fluxes estimated from microstructure profiles are much too weak  
582 to balance the upwelling transports inferred by uniformly-extrapolated moored velocity es-  
583 timates (Thurnherr et al. 2005).

584 Our quasi-realistic simulations provide the first BBL- and submesoscale-resolving simula-  
585 tions of the mixing-driven abyssal overturning in the Brazil Basin, complementing Huang  
586 and Jin (2002) and Ogden and Ferrari’s (in prep) coarser-resolution basin-scale simulations.  
587 Despite the idealization of our numerical set-up, we qualitatively reproduce key features of  
588 the observations: broad up-slope flow and near-boundary stratification of  $B_z \approx \mathcal{O}(10^{-7}\text{s}^{-2})$   
589 along the canyon trough (Toole 2007; Ledwell et al. 2000), stronger near-bottom stratifi-  
590 cation along the hills surrounding the canyon (Polzin 2009), hydraulically accelerated flow  
591 over blocking sills (Clément et al. 2017), and the mean diapycnal downwelling and spreading  
592 of a tracer released in the SML (Ledwell et al. 2000; see companion manuscript Drake et  
593 al., in prep.). Despite this qualitative agreement, the simulated diapycnal transports within  
594 the canyon are too weak—and the stratification too strong—by roughly a factor of 2. These  
595 remaining discrepancies could be explained by the previously mentioned limitations of the  
596 inherently local slope-aligned modelling framework and the self-similar parameterization of  
597 small-scale mixing. The lack of full equilibration of the simulations could explain the too-  
598 strong stratification—the 1D models become about half as stratified at equilibrium—but not  
599 the too-weak up-canyon flow. Too-weak canyon mixing, on the other hand, could potentially  
600 explain both biases: we speculate that microstructure-based estimates of the turbulent dif-  
601 fusivity may be biased low due to sampling biases (Watson et al. 1988; Voet et al. 2015; Cael

602 and Mashayek 2021; Whalen 2021) or biases in the mixing parameterization (Ijichi et al.  
 603 2020). Based on observations and basin-scale simulations of tracer spreading, respectively,  
 604 Ledwell (in prep) and Ogden and Ferrari (in prep) similarly conclude that tracer observa-  
 605 tions are more consistent with diffusivities about 2 times larger than those inferred from  
 606 microstructure<sup>8</sup>.

607 The characteristic topographic features in the BBTRE (large-scale slope, canyon, and hills)  
 608 are typical of mid-ocean ridges, such that the dynamics described here can be thought to  
 609 apply to the global mid-ocean ridge system (with the steepness of slopes and hills modulated  
 610 by the age of the rift valley and the Coriolis parameter by its latitude). The BBTRE simula-  
 611 tion exhibits an instantaneous diapycnal upwelling transport in the BBL of  $\mathcal{E}_{\text{BBL}} = 60 \text{ mSv}$ ,  
 612 where  $\mathcal{E} = \frac{1}{\Delta b} \int_{\mathcal{V}(|b-b'| < \Delta b/2)} \nabla \cdot (\kappa \nabla b') dV$  is the average watermass transformation rate within  
 613 a volume  $\mathcal{V}$  for a layer of thickness  $\Delta b$  and  $\mathcal{E}_{\text{BBL}}$  confines this integral strictly to regions  
 614 of buoyancy flux convergence (see the companion manuscript Drake et al.). The upwelling  
 615 transport suggested by the bulk buoyancy budget presented here (Figure 8f) is smaller than  
 616  $\mathcal{E}_{\text{BBL}}$  by a factor of three due to substantial cancellation from temporal averaging and oppos-  
 617 ing cross-slope flows at the same height above the mean slope (e.g. Figure 4a). Extrapolating  
 618 these BBL watermass transformations to the length of the Mid-Atlantic Ridge in the Brazil  
 619 Basin (about 55 times the domain width  $L_y = 60 \text{ km}$ ), this 3.3 Sv of BBL upwelling<sup>9</sup> would  
 620 alone balance much of the 3.7–4.0 Sv net inflow of Antarctic Bottom Water in the Brazil  
 621 Basin (Hogg et al. 1982; Morris et al. 2001). Extrapolating even further to a global mid-

---

<sup>8</sup>Given the uncertainties of the microstructure methods, agreement within a factor of 2 is generally considered to be good (e.g. Gregg et al. 2018).

<sup>9</sup>This is much larger than Ruan and Callies' (2020) estimate of 0.5 Sv because our near-bottom stratification on the ridge flanks is much stronger than theirs, due to a combination of restratification effect of abyssal hills and fundamental differences between the slope-aligned and transient model configurations (see Peterson and Callies 2021).

ocean ridge system of length  $80 \times 10^3$  km (including both flanks of the ridge; Thurnherr et al. 2005) leads to a global BBL upwelling of 80 Sv due to upwelling along mid-ocean ridges, roughly consistent with global diagnostic estimates of BBL upwelling (Ferrari et al. 2016; McDougall and Ferrari 2017).

Global extrapolations of localized estimates of BBL upwelling, such as the above, have been used to attribute the *net* abyssal overturning to individual mixing hotspots (e.g. Ferron et al. 1998; Voet et al. 2015; Thurnherr et al. 2020; Spingys et al. 2021). These observations, however, generally also imply significant downwelling in adjacent buoyancy classes, suggesting that their localized upwelling may be offset by a similar dynamical process operating nearby—but centered on a different buoyancy surface. For example, Thurnherr et al. (2020) argue that the observed turbulent buoyancy flux convergence in the BBTRE canyon, extrapolated to all of the fracture zone canyons in the Brazil Basin, is sufficient to transform “the total inflow of AABW”. Above the canyon, however, their own observations imply an opposing buoyancy flux divergence of comparable magnitude; upwelling within the canyon is thus only half of the story. Consider the following heuristic argument which applies the slope-aligned buoyancy budgets derived in Section 2c in buoyancy coordinates. Following the  $\gamma_n \in \{28.1, 28.15\}$  kg/m<sup>3</sup> neutral density class in Thurnherr et al.’s (2020) Figure 3, for example, we apply eq. (16) to their integrated buoyancy fluxes in Figure 7 to infer a bulk upwelling of  $\Psi(z_{\text{crest}}) \simeq \frac{\langle wb \rangle / L_x}{N^2 \sin \theta} \simeq \frac{\Gamma \int \epsilon \, dy}{N^2 \sin \theta} \approx \frac{0.2 (2 \times 10^{-5} \text{ m}^3/\text{s}^3)}{(1 \times 10^{-6} \text{ s}^{-2})(2 \times 10^{-3})} = 10 \text{ mSv}$  within the canyon at the DoMORE site<sup>10</sup>. This confirms Thurnherr et al.’s (2020) central conclusion that—regardless of the shape of individual buoyancy flux profiles—the concave canyon topography implies that the *integrated* flux peaks at the crest of the canyon and thus drives a substantial bulk upwelling within the canyon. A few hundred km down-canyon, however, this same

---

<sup>10</sup>Averaging the overflow and non-overflow profiles, for simplicity.

645 density class rests above the canyon and experiences a net buoyancy flux divergence, driving  
 646 a downwelling of  $\Psi(z_{\text{crest}} + 500 \text{ m}) - \Psi(z_{\text{crest}}) \approx -4 \text{ mSv}$  that partially compensates for the  
 647 upwelling in the canyon and suggests a significantly weaker *net* upwelling of 6 mSv for the  
 648 BBTRE canyon. This heuristic exercise serves as a cautionary tale for attributing abyssal  
 649 upwelling to individual regions or processes: both strictly positive and strictly negative com-  
 650 ponents of watermass transformations along a buoyancy surface must be accounted for to  
 651 robustly characterize the net overturning circulation.

652 At a global scale, diagnostic estimates of watermass transformations suggest significant  
 653 compensation is the norm, exhibiting typical amplification factors of  $\mathcal{A} \equiv \mathcal{E}_{\text{BBL}}/\mathcal{E}$  of 2 to  
 654 5, where  $\mathcal{E} = \mathcal{E}_{\text{BBL}} + \mathcal{E}_{\text{SML}}$  is the net diapycnal transport and  $\mathcal{E}_{\text{SML}}$  is the downwelling in  
 655 the stratified mixing layer (Ferrari et al. 2016; McDougall and Ferrari 2017; Cimoli et al.  
 656 2019). However, these diagnostic exercises do not provide any insight into the physics  
 657 underlying the observed density structure that supports these transformations. More prob-  
 658 lematically, these results seem to contradict the weak upwelling with  $\mathcal{A} \simeq 1$  implied by 1D  
 659 boundary layer dynamics (Section 2b). Building upon Callies (2018) and Ruan and Callies  
 660 (2020), our prognostic modelling approach demonstrates how three-dimensional eddy and  
 661 topographic effects conspire to provide sufficient restratification to support a significant up-  
 662 welling/downwelling dipole, i.e.  $\mathcal{A} \gg 1$  (Figure 8a,f). Our results inspire two open questions:  
 663 1) which topographic regimes (e.g. ridges, slopes, plains) or topographic roughness features  
 664 (e.g. hills, canyons, channels, sills, or seamounts) contribute the most to abyssal watermass  
 665 transformations (e.g. Armi and D’Asaro 1980; Bryden and Nurser 2003; Thurnherr et al.  
 666 2005; Legg et al. 2009; Nazarian et al. 2021; Mashayek et al. 2021) and 2) what are the dy-  
 667 namics that support finite watermass transformations in these regions (Garrett 1979, 1990;  
 668 Callies 2018; Drake et al. 2020)?

669 Our combined assumptions of constant background stratification and zero barotropic cross-  
 670 slope pressure gradient assert that the net upwelling scales with the background diffusivity  
 671 (eq. 13) and thus that the net upwelling  $\Psi_\infty = \mathcal{E}$  is very small. While our local model helps  
 672 explain the magnitude of bottom boundary layer upwelling  $\mathcal{E}_{\text{BBL}}$ , it does not meaningfully  
 673 constrain  $\mathcal{E}_{\text{SML}}$  or  $\mathcal{A}$ . Salmun et al. (1991) use asymptotic analysis to show that small  
 674 perturbations away from a constant interior stratification drive an exchange flow between  
 675 the boundary and the interior, which then feeds back on the interior stratification. In the  
 676 context of the abyssal ocean, vertical variations in the basin-scale interior stratification are  
 677 relatively large, such that they enter as leading-order terms in watermass transformations  
 678 (Spingys et al. 2021) and drive substantial exchange between the mixing layers and the  
 679 interior (Holmes et al. 2018). In Drake et al.’s (2020) idealized basin-scale simulations,  
 680 this boundary–interior coupling results in a substantial reduction of  $\mathcal{E}_{\text{SML}}$ , permitting an  
 681 amplification factor of  $\mathcal{A} = 1.5$  much smaller than the  $\mathcal{A} \gg 1$  governed by local dynamics.  
 682 These idealized prognostic model results are qualitatively consistent with the diagnostic  
 683 approaches described above, but quantitative understanding of  $\mathcal{E}_{\text{BBL}}$ ,  $\mathcal{E}_{\text{SML}}$ , and  $\mathcal{A}$  remains  
 684 incomplete.

685 Understanding of bottom-enhanced mixing has advanced considerably in recent years due  
 686 to a combination of breakthroughs in observation (e.g. Polzin et al. 1997; Ledwell et al.  
 687 2000), theory (e.g. Polzin 2009), and modelling (e.g. Nikurashin and Legg 2011). The  
 688 interpretation of these results in terms of broad diapycnal downwelling in the SML atop  
 689 vigorous diapycnal upwelling in a BBL (Ferrari et al. 2016), however, is challenged by higher-  
 690 resolution observations (van Haren 2018; Naveira Garabato et al. 2019; Polzin et al. 2021)  
 691 and simulations (Gayen and Sarkar 2011; Kaiser 2020) of mixing processes within the bottom  
 692 few dozen meters of the ocean. In addition to the debate on the nature of boundary mixing

693 itself (see Polzin and McDougall 2022), the role of the resulting boundary layer flows in the  
694 global overturning circulation remains shrouded by poor understanding of their coupling to  
695 the far-field interior (Drake et al. 2020; Peterson and Callies 2021).

696 *Acknowledgments.* We thank the crews of the BBTRE and DoMORE field campaigns for  
697 collecting the observations that motivated this work. We acknowledge funding support from  
698 National Science Foundation Awards 6932401 and 6936732. This material is based upon  
699 work supported by the National Science Foundation Graduate Research Fellowship Program  
700 under Grant No. 174530. Any opinions, findings, and conclusions or recommendations  
701 expressed in this material are those of the author(s) and do not necessarily reflect the  
702 views of the National Science Foundation. This research is also supported by the NOAA  
703 Climate and Global Change Postdoctoral Fellowship Program, administered by UCAR’s  
704 Cooperative Programs for the Advancement of Earth System Science (CPAESS) under award  
705 #NA18NWS4620043B.

706 *Data availability statement.* The source code for the MITgcm simulations and all of the  
707 Python code necessary to produce the figures will be publicly available at [github.com/  
708 hdrake/sim-bbtre](https://github.com/hdrake/sim-bbtre) upon acceptance (or earlier by requesting the corresponding author).  
709 Our analysis of labeled data arrays is greatly simplified by the `xarray` package in Python  
710 (Hoyer and Hamman 2017).

## 711 APPENDIX

### 712 **One-dimensional model of restratification by submesoscale baroclinic eddies** 713 **along a sloping boundary**

714 Our goal is to reformulate the 1D sloping BBL model using Transformed Eulerian Mean  
715 (TEM) theory (Andrews and McIntyre 1976) to facilitate the inclusion of submesoscale eddy  
716 restratification. We begin by assuming there are no large-scale variations in the perturba-  
717 tions, so that we can average in the along-slope ( $y$ ) and cross-slope ( $x$ ) directions and drop  
718 cross- and along-slope gradients. Then, averaging the slope-aligned equations (1–5) in both  
719  $x$  and  $y$ , we have

$$\bar{u}_t - f\bar{v} \cos \theta - \bar{b} \sin \theta - \partial_z (\kappa \bar{u}_z) = -\partial_z (\overline{w'u'}), \quad (\text{A1})$$

$$\bar{v}_t + f\bar{u} \cos \theta - \partial_z (\kappa \bar{v}_z) = -\partial_z (\overline{w'v'}), \quad (\text{A2})$$

$$\bar{p}_z - \bar{b} \cos \theta = 0, \quad (\text{A3})$$

$$\bar{b}_t + \bar{u} N^2 \sin \theta - \partial_z (\kappa \bar{B}_z) = -\partial_z (\overline{w'b'}), \quad (\text{A4})$$

720 where the eddy fluctuations  $\phi' \equiv \phi - \bar{\phi}$  are departures from the slope-average means  $\bar{\phi}$ ,  
721  $\bar{w} = 0$  from continuity and the no-flux bottom boundary condition, and we assume  $\sigma = 1$ .

722 We introduce the residual velocities

$$(u^\dagger, w^\dagger) \equiv (\bar{u}, \bar{w}) + (-\partial_z, \partial_x) \psi_e, \quad (\text{A5})$$

723 which add to the Eulerian mean flow  $\bar{\mathbf{u}}$  an eddy-induced overturning  $\nabla \times \mathbf{y}\psi_e$  in the  $(x, z)$   
724 plane that is by definition also non-divergent.

725 Using a convenient definition of the eddy streamfunction (Plumb and Ferrari 2005), in-  
726 spired by Andrews and McIntyre (1976) but in a slightly rotated coordinate frame,

$$\psi_e \equiv \frac{\overline{u'b'}}{\overline{B_z}}, \quad (\text{A6})$$

727 we express the slope-averaged equations (A1–A4) in terms of the residual circulation  $\mathbf{u}^\dagger =$   
728  $(u^\dagger, \bar{v}, w^\dagger)$ . Since, by assumption, the large-scale average solution is independent of  $x$ , we  
729 have  $\partial_x \psi_e = 0$  and thus  $w^\dagger = \bar{w} = 0$ . The choice of the eddy streamfunction (A6) eliminates

730 the cross-slope eddy buoyancy flux divergence term from the buoyancy equation<sup>11</sup> and we  
 731 are left with

$$\bar{v}_t + f u^\dagger \cos \theta - \partial_z (\kappa \bar{v}_z) = -\partial_z \left( \overline{w'v'} + f \cos \theta \frac{\overline{u'b'}}{\bar{B}_z} \right), \quad (\text{A7})$$

$$\bar{b}_t + u^\dagger N^2 \sin \theta - \partial_z (\kappa \bar{B}_z) = -\partial_z \left[ \frac{\overline{\mathbf{u}'b' \cdot \nabla \bar{B}}}{\bar{B}_z} \right], \quad (\text{A8})$$

732 where we recall the total buoyancy is decomposed as  $B \equiv N^2 \hat{z} + \bar{b} + b'$ . The mean slope of  
 733 isopycnals in the rotated reference frame is given by  $-\bar{B}_x/\bar{B}_z = -N^2 \sin \theta / (N^2 \cos \theta + \bar{b}_z)$   
 734 because  $\bar{b}$  is independent of  $x$ . Thus we identify the eddy flux term in the buoyancy budget  
 735 as proportional to the flux across a mean density surface,

$$\overline{\mathbf{u}'b'} \cdot \frac{\nabla \bar{B}}{|\nabla \bar{B}|} \propto \overline{\mathbf{u}'b'} \cdot \nabla \bar{B} \simeq 0, \quad (\text{A9})$$

736 which is vanishingly small because the submesoscale eddies are characterized by large  
 737 Richardson numbers and do not generate mixing across density surfaces (Figure 11b). Then,  
 738 at leading order,

$$\bar{b}_t + u^\dagger N^2 \sin \theta - \partial_z (\kappa \bar{B}_z) = 0, \quad (\text{A10})$$

739 and the eddy closure problem is confined to the residual along-slope momentum flux (A7).  
 740 Equation (A10) clarifies that the residual velocity  $\mathbf{u}^\dagger$  is in fact the Lagrangian velocity that  
 741 advects tracers, which is one of the advantages of the TEM framework.

742 Assuming quasi-geostrophic scaling for the eddy fluxes, the Reynolds flux term in (A7)  
 743 is  $\mathcal{O}(R_o)$  smaller than the buoyancy flux term and can be neglected. Closing the system  
 744 then only requires a closure for the cross-slope eddy buoyancy flux  $\overline{u'b'}$  that appears in  
 745 the  $y$ -momentum equation. Following the GM eddy parameterization scheme (Gent and  
 746 McWilliams 1990; Gent et al. 1995), we assume that the truly horizontal buoyancy flux is

---

<sup>11</sup>This property is useful in the general case, but in the present slope-aligned framework the horizontal fluxes are already eliminated by along-slope averaging.

747 down-gradient,

$$\overline{\hat{u}'b'} \simeq -K(z)\overline{B_{\hat{x}}}, \quad (\text{A11})$$

748 such that it acts to flatten sloping isopycnal thereby releasing available potential energy,  
 749 as expected from baroclinic instability theory. Re-expressed in slope coordinates, the only  
 750 component of the horizontal buoyancy gradient that survive the large-scale averaging is the  
 751 slope-normal gradient of the perturbation buoyancy,  $\overline{B_{\hat{x}}} = -\overline{b_z} \sin \theta$ , such that

$$K(z) = -\frac{\overline{\hat{u}'b'}}{\overline{B_{\hat{x}}}} = -\frac{\overline{u'b'} \cos \theta - \overline{w'b'} \sin \theta}{-\overline{b_z} \sin \theta} = \frac{\overline{u'b'}}{\overline{B_z}} \frac{N^2 + \overline{b_z} \cos \theta}{\overline{b_z} \sin \theta}, \quad (\text{A12})$$

752 where we use the chain rule to express  $K$  in terms of slope-aligned fluxes and gradients only,  
 753 have invoked (A9), and recall that  $\overline{B_z} = N^2 + \overline{b_z} \cos \theta$  is the true-vertical buoyancy gradient.

754 To clarify the role of this additional eddy-induced overturning, we focus on the stratified  
 755 interior above the frictional bottom layer, where we assume geostrophic balance applies in the  
 756 cross-slope ( $\mathbf{y}$ ) momentum equation only (as in semi-geostrophic theories of frontogenesis),

$$-f\overline{v_z} \cos \theta = \overline{b_z} \sin \theta. \quad (\text{A13})$$

757 Combining (A12) and (A13) and plugging back into (A7) yields

$$\overline{v_t} + fu^\dagger \cos \theta = \partial_z (\nu_e(z)\overline{v_z}), \quad (\text{A14})$$

758 where we define

$$\nu_e(z) \equiv \sigma_v(z)\kappa(z) \quad \text{with} \quad \sigma_v(z) \equiv 1 + \frac{K(z)}{\kappa(z)} \frac{f^2}{\overline{B_z}} \cos^2 \theta \quad (\text{A15})$$

759 as an enhanced vertical momentum diffusion (as in Greatbatch and Lamb 1990 but mod-  
 760 ified by the geometric factor  $\cos^2 \theta$ , which approaches unity for shallow slopes). In the  
 761 planetary geostrophic limit, enhanced vertical momentum diffusion is also equivalent to a  
 762 down-gradient isopycnal flux of potential vorticity (Rhines and Young 1982).

763 Although we have shown that the slope-averaged equations can be closed by invoking  
764 a submesoscale eddy diffusivity parameter  $K(z)$ , the parameterization is incomplete since  
765 we have not specified its magnitude or structure in terms of only resolved quantities and  
766 external parameters. Developing such a parameterization is beyond the scope of this pa-  
767 per; however, we can explore the impact of such a parameterization by directly diagnosing  
768 the eddy fluxes—and the resulting effective eddy diffusivity (A12)—from the Smooth3D  
769 simulation and plugging it back into the corresponding 1D model.

770 Using this closure, the 1D sloping BBL model for the residual circulation is given by

$$u_t^\dagger - f\bar{v} \cos \theta = \bar{b} \sin \theta + \partial_z (\kappa u_z^\dagger), \quad (\text{A16})$$

$$\bar{v}_t + f u^\dagger \cos \theta = \partial_z (\sigma_v(z) \kappa \bar{v}_z), \quad (\text{A17})$$

$$w^\dagger = 0 \quad (\text{A18})$$

$$\bar{p}_z = \bar{b} \cos \theta, \quad (\text{A19})$$

$$\bar{b}_t + u^\dagger N^2 \sin \theta = \partial_z [\kappa (N^2 \cos \theta + \bar{b}_z)], \quad (\text{A20})$$

771 which is identical to the canonical 1D sloping BBL model (8–10) for the Eulerian mean  
772 circulation except for the enhancement of vertical diffusion of along-slope momentum by a  
773 factor  $\sigma_v(z)$ . Figure 11a shows how the effective vertical Prandtl number can be approxi-  
774 mated by a simple vertical structure,  $\sigma_v(z) \propto z \exp\{-z/\eta\}$  with an optimal vertical scale of  
775  $\eta = 225 \text{ m} \approx h$  and a peak magnitude of  $\sigma_v = \mathcal{O}(100)$ , dramatically enhancing the vertical  
776 diffusion of the along-slope thermal wind. This form satisfies  $\sigma_v \rightarrow 1$  as  $z \rightarrow 0$ , such that the  
777 eddy-induced flow does not interfere with the bottom boundary conditions on the Eulerian  
778 mean flow.

779 Figure 1 and Figures 8a,b,c show the impact of this momentum diffusion on the 1D BBL  
780 solution and its buoyancy budget, respectively. Callies (2018) and Holmes et al. (2019) pro-

781 pose conceptually similar parameterizations, but omit the derivation and assume a vertically-  
782 uniform enhancement of the Prandtl number  $\sigma = 230$ , which distorts the vertical structure  
783 of submesoscale eddy restratification.

## 784 **References**

785 Andrews, D. G., and M. E. McIntyre, 1976: Planetary Waves in Horizontal and Vertical  
786 Shear: The Generalized Eliassen-Palm Relation and the Mean Zonal Acceleration. *Journal*  
787 *of the Atmospheric Sciences*, **33** (11), 2031–2048, doi:10.1175/1520-0469(1976)033<2031:  
788 PWIHAV>2.0.CO;2, publisher: American Meteorological Society.

789 Armi, L., 1978: Some evidence for boundary mixing in the deep Ocean. *Journal of Geophys-*  
790 *ical Research*, **83** (C4), 1971, doi:10.1029/JC083iC04p01971, URL [http://doi.wiley.com/  
791 10.1029/JC083iC04p01971](http://doi.wiley.com/10.1029/JC083iC04p01971).

792 Armi, L., 1979a: Effects of variations in eddy diffusivity on property distributions in the  
793 oceans. *Journal of Marine Research*, **37** (3), 515–530, URL [https://escholarship.org/uc/  
794 item/65g216cr](https://escholarship.org/uc/item/65g216cr).

795 Armi, L., 1979b: Reply to Comments by C. Garrett. *Journal of Geophysical Re-*  
796 *search*, **84** (C8), 5097, doi:10.1029/JC084iC08p05097, URL [http://doi.wiley.com/10.  
797 1029/JC084iC08p05097](http://doi.wiley.com/10.1029/JC084iC08p05097), publisher: Wiley-Blackwell.

798 Armi, L., and E. D’Asaro, 1980: Flow structures of the benthic ocean. *Journal of Geophys-*  
799 *ical Research: Oceans*, **85** (C1), 469–484, doi:<https://doi.org/10.1029/JC085iC01p00469>,  
800 URL <https://agupubs.onlinelibrary.wiley.com/doi/abs/10.1029/JC085iC01p00469>,  
801 \_eprint: <https://agupubs.onlinelibrary.wiley.com/doi/pdf/10.1029/JC085iC01p00469>.

802 Baines, P. G., 1979: Observations of stratified flow past Three-dimensional barriers. *Journal*  
803 *of Geophysical Research: Oceans*, **84 (C12)**, 7834–7838, doi:10.1029/JC084iC12p07834,  
804 URL <https://agupubs.onlinelibrary.wiley.com/doi/abs/10.1029/JC084iC12p07834>,  
805 \_eprint: <https://agupubs.onlinelibrary.wiley.com/doi/pdf/10.1029/JC084iC12p07834>.

806 Boccaletti, G., R. Ferrari, and B. Fox-Kemper, 2007: Mixed Layer Instabilities and Restrat-  
807 ification. *Journal of Physical Oceanography*, **37 (9)**, 2228–2250, doi:10.1175/JPO3101.1,  
808 URL <http://journals.ametsoc.org/doi/abs/10.1175/JPO3101.1>.

809 Bryden, H. L., and A. J. G. Nurser, 2003: Effects of Strait Mixing on Ocean Stratifica-  
810 tion. *Journal of Physical Oceanography*, **33 (8)**, 1870–1872, doi:10.1175/1520-0485(2003)  
811 033(1870:EOSMOO)2.0.CO;2, URL [https://journals.ametsoc.org/view/journals/phoc/](https://journals.ametsoc.org/view/journals/phoc/33/8/1520-0485_2003_033_1870_eosmoo_2.0.co_2.xml)  
812 [33/8/1520-0485\\_2003\\_033\\_1870\\_eosmoo\\_2.0.co\\_2.xml](https://journals.ametsoc.org/view/journals/phoc/33/8/1520-0485_2003_033_1870_eosmoo_2.0.co_2.xml), publisher: American Meteorological  
813 Society Section: Journal of Physical Oceanography.

814 Burns, K. J., G. M. Vasil, J. S. Oishi, D. Lecoanet, and B. Brown, 2016: Dedalus: Flexible  
815 framework for spectrally solving differential equations. *Astrophysics Source Code Library*,  
816 *record ascl:1603.015*, URL <http://adsabs.harvard.edu/abs/2016ascl.soft03015B>.

817 Cael, B., and A. Mashayek, 2021: Log-Skew-Normality of Ocean Turbulence. *Physical*  
818 *Review Letters*, **126 (22)**, 224 502, doi:10.1103/PhysRevLett.126.224502, URL <https://link.aps.org/doi/10.1103/PhysRevLett.126.224502>, publisher: American Physical So-  
819 ciety.  
820

821 Callies, J., 2018: Restratification of Abyssal Mixing Layers by Submesoscale Baroclinic Ed-  
822 dies. *Journal of Physical Oceanography*, JPO–D–18–0082.1, doi:10.1175/JPO-D-18-0082.  
823 1, URL <http://journals.ametsoc.org/doi/10.1175/JPO-D-18-0082.1>.

824 Callies, J., and R. Ferrari, 2018: Dynamics of an Abyssal Circulation Driven by Bottom-  
825 Intensified Mixing on Slopes. *Journal of Physical Oceanography*, **48** (6), 1257–1282, doi:10.  
826 1175/JPO-D-17-0125.1, URL [http://journals.ametsoc.org/doi/10.1175/JPO-D-17-0125.](http://journals.ametsoc.org/doi/10.1175/JPO-D-17-0125.1)  
827 1.

828 Cimoli, L., C.-c. P. Caulfield, H. L. Johnson, D. P. Marshall, A. Mashayek, A. C. N. Gara-  
829 bato, and C. Vic, 2019: Sensitivity of deep ocean mixing to local internal tide breaking and  
830 mixing efficiency. *Geophysical Research Letters*, **n/a** (n/a), doi:10.1029/2019GL085056,  
831 URL <https://agupubs.onlinelibrary.wiley.com/doi/abs/10.1029/2019GL085056>.

832 Clément, L., A. M. Thurnherr, and L. C. St. Laurent, 2017: Turbulent Mixing in a  
833 Deep Fracture Zone on the Mid-Atlantic Ridge. *Journal of Physical Oceanography*,  
834 **47** (8), 1873–1896, doi:10.1175/JPO-D-16-0264.1, URL [http://journals.ametsoc.org/doi/](http://journals.ametsoc.org/doi/10.1175/JPO-D-16-0264.1)  
835 [10.1175/JPO-D-16-0264.1](http://journals.ametsoc.org/doi/10.1175/JPO-D-16-0264.1).

836 de Lavergne, C., G. Madec, J. Le Sommer, A. J. G. Nurser, and A. C. Naveira Garabato,  
837 2016: On the Consumption of Antarctic Bottom Water in the Abyssal Ocean. *Journal*  
838 *of Physical Oceanography*, **46** (2), 635–661, doi:10.1175/JPO-D-14-0201.1, URL [http:](http://journals.ametsoc.org/doi/10.1175/JPO-D-14-0201.1)  
839 [//journals.ametsoc.org/doi/10.1175/JPO-D-14-0201.1](http://journals.ametsoc.org/doi/10.1175/JPO-D-14-0201.1).

840 de Lavergne, C., and Coauthors, 2020: A Parameterization of Local and  
841 Remote Tidal Mixing. *Journal of Advances in Modeling Earth Systems*,  
842 **12** (5), e2020MS002065, doi:<https://doi.org/10.1029/2020MS002065>, URL  
843 <https://agupubs.onlinelibrary.wiley.com/doi/abs/10.1029/2020MS002065>, eprint:  
844 <https://agupubs.onlinelibrary.wiley.com/doi/pdf/10.1029/2020MS002065>.

- 845 Dell, R., and L. Pratt, 2015: Diffusive boundary layers over varying topography. *Journal*  
846 *of Fluid Mechanics*, **769**, 635–653, doi:10.1017/jfm.2015.88, URL [http://www.journals.](http://www.journals.cambridge.org/abstract_S0022112015000889)  
847 [cambridge.org/abstract\\_S0022112015000889](http://www.journals.cambridge.org/abstract_S0022112015000889).
- 848 Dell, R. W., 2013: *Boundary layer dynamics and deep ocean mixing in Mid-Atlantic Ridge*  
849 *canyons*. Massachusetts Institute of Technology and Woods Hole Oceanographic Institu-  
850 tion, Woods Hole, MA, doi:10.1575/1912/5740, URL <https://hdl.handle.net/1912/5740>.
- 851 Drake, H. F., 2021: Control of the abyssal ocean overturning circulation by mixing-  
852 driven bottom boundary layers. Thesis, Massachusetts Institute of Technology and  
853 Woods Hole Oceanographic Institution, doi:10.1575/1912/27424, URL [https://darchive.](https://darchive.mblwhoilibrary.org/handle/1912/27424)  
854 [mblwhoilibrary.org/handle/1912/27424](https://darchive.mblwhoilibrary.org/handle/1912/27424), accepted: 2021-08-10T15:07:15Z.
- 855 Drake, H. F., R. Ferrari, and J. Callies, 2020: Abyssal Circulation Driven  
856 by Near-Boundary Mixing: Water Mass Transformations and Interior Strat-  
857 ification. *Journal of Physical Oceanography*, **50** (8), 2203–2226, doi:10.1175/  
858 JPO-D-19-0313.1, URL [https://journals.ametsoc.org/jpo/article/50/8/2203/348530/](https://journals.ametsoc.org/jpo/article/50/8/2203/348530/Abyssal-Circulation-Driven-by-Near-Boundary-Mixing)  
859 [Abyssal-Circulation-Driven-by-Near-Boundary-Mixing](https://journals.ametsoc.org/jpo/article/50/8/2203/348530/Abyssal-Circulation-Driven-by-Near-Boundary-Mixing), publisher: American Meteorolog-  
860 ical Society.
- 861 Ferrari, R., 2014: What goes down must come up. *Nature*, **513**, 179–180.
- 862 Ferrari, R., A. Mashayek, T. J. McDougall, M. Nikurashin, and J.-M. Campin, 2016: Turning  
863 Ocean Mixing Upside Down. *Journal of Physical Oceanography*, **46** (7), 2239–2261, doi:10.  
864 1175/JPO-D-15-0244.1, URL [http://journals.ametsoc.org/doi/10.1175/JPO-D-15-0244.](http://journals.ametsoc.org/doi/10.1175/JPO-D-15-0244.1)  
865 1.

866 Ferrari, R., and R. Plumb, 2003: Residual circulation in the ocean. *Near-Boundary Processes*  
867 *and Their Parameterization: Proc. 'Aha Huliko'a Hawaiian Winter Workshop*, 219–228.

868 Ferron, B., H. Mercier, K. Speer, A. Gargett, and K. Polzin, 1998: Mixing in the Romanche  
869 Fracture Zone. *Journal of Physical Oceanography*, **28** (10), 1929–1945, doi:10.1175/  
870 1520-0485(1998)028(1929:MITRFZ)2.0.CO;2, URL [https://journals.ametsoc.org/view/  
871 journals/phoc/28/10/1520-0485\\_1998\\_028\\_1929\\_mitr fz\\_2.0.co.2.xml](https://journals.ametsoc.org/view/journals/phoc/28/10/1520-0485_1998_028_1929_mitr fz_2.0.co.2.xml), publisher: American  
872 Meteorological Society Section: Journal of Physical Oceanography.

873 Fox-Kemper, B., R. Ferrari, and R. Hallberg, 2008: Parameterization of Mixed Layer Ed-  
874 dies. Part I: Theory and Diagnosis. *Journal of Physical Oceanography*, **38** (6), 1145–  
875 1165, doi:10.1175/2007JPO3792.1, URL [http://journals.ametsoc.org/doi/abs/10.1175/  
876 2007JPO3792.1](http://journals.ametsoc.org/doi/abs/10.1175/2007JPO3792.1).

877 Garrett, C., 1979: Comment on ‘Some evidence for boundary mixing in the deep  
878 ocean’ by Laurence Armi. *Journal of Geophysical Research*, **84** (C8), 5095, doi:  
879 10.1029/JC084iC08p05095, URL <http://doi.wiley.com/10.1029/JC084iC08p05095>, pub-  
880 lisher: Wiley-Blackwell.

881 Garrett, C., 1990: The role of secondary circulation in boundary mixing. *Journal of Geo-  
882 physical Research*, **95** (C3), 3181, doi:10.1029/JC095iC03p03181, URL [http://doi.wiley.  
883 com/10.1029/JC095iC03p03181](http://doi.wiley.com/10.1029/JC095iC03p03181), publisher: Wiley-Blackwell.

884 Garrett, C., P. MacCready, and P. Rhines, 1993: Boundary Mixing and Arrested Ekman  
885 Layers: Rotating Stratified Flow Near a Sloping Boundary. *Annual Review of Fluid Me-  
886 chanics*, **25** (1), 291–323, doi:10.1146/annurev.fl.25.010193.001451, URL [http://www.  
887 annualreviews.org/doi/10.1146/annurev.fl.25.010193.001451](http://www.annualreviews.org/doi/10.1146/annurev.fl.25.010193.001451), publisher: Annual Reviews  
888 4139 El Camino Way, P.O. Box 10139, Palo Alto, CA 94303-0139, USA.

- 889 Gayen, B., and S. Sarkar, 2011: Negative turbulent production during flow reversal in a strat-  
890 ified oscillating boundary layer on a sloping bottom. *Physics of Fluids*, **23** (10), 101 703,  
891 doi:10.1063/1.3651359, URL <https://aip.scitation.org/doi/10.1063/1.3651359>, publisher:  
892 American Institute of Physics.
- 893 Gent, P. R., and J. C. McWilliams, 1990: Isopycnal Mixing in Ocean Cir-  
894 culation Models. *Journal of Physical Oceanography*, **20** (1), 150–155, doi:10.  
895 1175/1520-0485(1990)020<0150:IMIOCM>2.0.CO;2, URL [http://journals.ametsoc.org/  
896 doi/abs/10.1175/1520-0485\(1990\)020%3C0150:IMIOCM%3E2.0.CO;2](http://journals.ametsoc.org/doi/abs/10.1175/1520-0485(1990)020%3C0150:IMIOCM%3E2.0.CO;2), iSBN: 0022-3670.
- 897 Gent, P. R., J. Willebrand, T. J. McDougall, and J. C. McWilliams, 1995: Parameter-  
898 izing Eddy-Induced Tracer Transports in Ocean Circulation Models. *Journal of Phys-  
899 ical Oceanography*, **25** (4), 463–474, doi:10.1175/1520-0485(1995)025<0463:PEITTI>2.0.  
900 CO;2, URL [https://journals.ametsoc.org/view/journals/phoc/25/4/1520-0485\\_1995\\_025\\_  
901 0463\\_peitti\\_2\\_0\\_co\\_2.xml](https://journals.ametsoc.org/view/journals/phoc/25/4/1520-0485_1995_025_0463_peitti_2_0_co_2.xml), publisher: American Meteorological Society Section: Journal of  
902 Physical Oceanography.
- 903 Gordon, A. L., 1986: Is there a global scale ocean circulation? *Eos, Transactions American  
904 Geophysical Union*, **67** (9), 109–110, doi:<https://doi.org/10.1029/EO067i009p00109>,  
905 URL <https://agupubs.onlinelibrary.wiley.com/doi/abs/10.1029/EO067i009p00109>,  
906 \_eprint: <https://agupubs.onlinelibrary.wiley.com/doi/pdf/10.1029/EO067i009p00109>.
- 907 Greatbatch, R. J., and K. G. Lamb, 1990: On Parameterizing Vertical Mixing of  
908 Momentum in Non-eddy Resolving Ocean Models. *Journal of Physical Oceanog-  
909 raphy*, **20** (10), 1634–1637, doi:10.1175/1520-0485(1990)020<1634:OPVMOM>2.0.  
910 CO;2, URL [https://journals.ametsoc.org/doi/abs/10.1175/1520-0485%281990%29020%  
911 3C1634%3AOPVMOM%3E2.0.CO%3B2](https://journals.ametsoc.org/doi/abs/10.1175/1520-0485%281990%29020%3C1634%3AOPVMOM%3E2.0.CO%3B2).

- 912 Gregg, M., E. D'Asaro, J. Riley, and E. Kunze, 2018: Mixing Efficiency in the Ocean. *Annual*  
913 *Review of Marine Science*, **10** (1), 443–473, doi:10.1146/annurev-marine-121916-063643,  
914 URL <http://www.annualreviews.org/doi/10.1146/annurev-marine-121916-063643>.
- 915 Gregg, M. C., 1987: Diapycnal mixing in the thermocline: A review. *Journal of Geophysical*  
916 *Research*, **92** (C5), 5249, doi:10.1029/JC092iC05p05249, URL [http://doi.wiley.com/10.](http://doi.wiley.com/10.1029/JC092iC05p05249)  
917 [1029/JC092iC05p05249](http://doi.wiley.com/10.1029/JC092iC05p05249).
- 918 Held, I. M., 2005: The gap between simulation and understanding in climate model-  
919 ing. *Bulletin of the American Meteorological Society*, **86** (11), 1609–1614, doi:10.1175/  
920 BAMS-86-11-1609, iISBN: 0003-0007.
- 921 Hogg, N., P. Biscaye, W. Gardner, and W. Jr, 1982: On the Transport and Modification of  
922 Antarctic Bottom Water in the Vema Channel. *J. Mar. Res.*, **40**, 231–263.
- 923 Holmes, R. M., C. de Lavergne, and T. J. McDougall, 2018: Ridges, Seamounts, Troughs,  
924 and Bowls: Topographic Control of the Diapycnal Circulation in the Abyssal Ocean.  
925 *Journal of Physical Oceanography*, **48** (4), 861–882, doi:10.1175/JPO-D-17-0141.1, URL  
926 <http://journals.ametsoc.org/doi/10.1175/JPO-D-17-0141.1>.
- 927 Holmes, R. M., C. de Lavergne, and T. J. McDougall, 2019: Tracer Transport within Abyssal  
928 Mixing Layers. *Journal of Physical Oceanography*, **49** (10), 2669–2695, doi:10.1175/  
929 JPO-D-19-0006.1, URL [https://journals.ametsoc.org/doi/full/10.1175/JPO-D-19-0006.](https://journals.ametsoc.org/doi/full/10.1175/JPO-D-19-0006.1)  
930 [1](https://journals.ametsoc.org/doi/full/10.1175/JPO-D-19-0006.1), publisher: American Meteorological Society.
- 931 Holmes, R. M., and T. J. McDougall, 2020: Diapycnal Transport near a Sloping  
932 Bottom Boundary. *Journal of Physical Oceanography*, **50** (11), 3253–3266, doi:10.  
933 [1175/JPO-D-20-0066.1](https://journals.ametsoc.org/view/journals/phoc/50/11/1175/JPO-D-20-0066.1), URL [https://journals.ametsoc.org/view/journals/phoc/50/11/](https://journals.ametsoc.org/view/journals/phoc/50/11/1175/JPO-D-20-0066.1)

934 jpoD200066.xml, publisher: American Meteorological Society Section: Journal of Physical  
935 Oceanography.

936 Hoyer, S., and J. Hamman, 2017: xarray: N-D labeled arrays and datasets in Python.  
937 *Journal of Open Research Software*, **5 (1)**, doi:10.5334/jors.148, URL [http://doi.org/10.](http://doi.org/10.5334/jors.148)  
938 [5334/jors.148](http://doi.org/10.5334/jors.148).

939 Huang, R. X., and X. Jin, 2002: Deep Circulation in the South Atlantic Induced by Bottom-  
940 Intensified Mixing over the Midocean Ridge\*. *Journal of Physical Oceanography*, **32 (4)**,  
941 1150–1164, doi:10.1175/1520-0485(2002)032<1150:DCITSA>2.0.CO;2.

942 Ijichi, T., L. S. Laurent, K. L. Polzin, and J. M. Toole, 2020: How  
943 Variable Is Mixing Efficiency in the Abyss? *Geophysical Research Let-*  
944 *ters*, **47 (7)**, e2019GL086813, doi:10.1029/2019GL086813, URL [https:](https://agupubs.onlinelibrary.wiley.com/doi/abs/10.1029/2019GL086813)  
945 [//agupubs.onlinelibrary.wiley.com/doi/abs/10.1029/2019GL086813](https://agupubs.onlinelibrary.wiley.com/doi/abs/10.1029/2019GL086813), eprint:  
946 <https://agupubs.onlinelibrary.wiley.com/doi/pdf/10.1029/2019GL086813>.

947 Kaiser, B. E., 2020: Finescale abyssal turbulence : sources and modeling. Thesis, Mas-  
948 sachusetts Institute of Technology, URL <https://dspace.mit.edu/handle/1721.1/128078>,  
949 accepted: 2020-10-18T21:45:36Z.

950 Kunze, E., 2017: The Internal-Wave-Driven Meridional Overturning Circulation. *Journal*  
951 *of Physical Oceanography*, **47 (11)**, 2673–2689, doi:10.1175/JPO-D-16-0142.1, URL [http:](http://journals.ametsoc.org/doi/10.1175/JPO-D-16-0142.1)  
952 [//journals.ametsoc.org/doi/10.1175/JPO-D-16-0142.1](http://journals.ametsoc.org/doi/10.1175/JPO-D-16-0142.1).

953 Kunze, E., E. Firing, J. M. Hummon, T. K. Chereskin, and A. M. Thurnherr, 2006:  
954 Global Abyssal Mixing Inferred from Lowered ADCP Shear and CTD Strain Profiles.  
955 *Journal of Physical Oceanography*, **36 (8)**, 1553–1576, doi:10.1175/JPO2926.1, URL

956 <https://journals.ametsoc.org/view/journals/phoc/36/8/jpo2926.1.xml>, publisher: Amer-  
957 ican Meteorological Society Section: Journal of Physical Oceanography.

958 Kunze, E., C. MacKay, E. E. McPhee-Shaw, K. Morrice, J. B. Girton, and S. R. Terker, 2012:  
959 Turbulent Mixing and Exchange with Interior Waters on Sloping Boundaries. *Journal*  
960 *of Physical Oceanography*, **42** (6), 910–927, doi:10.1175/JPO-D-11-075.1, URL [http://](http://journals.ametsoc.org/doi/abs/10.1175/JPO-D-11-075.1)  
961 [journals.ametsoc.org/doi/abs/10.1175/JPO-D-11-075.1](http://journals.ametsoc.org/doi/abs/10.1175/JPO-D-11-075.1).

962 Ledwell, J. R., E. T. Montgomery, K. L. Polzin, L. C. St. Laurent, R. W. Schmitt, and  
963 J. M. Toole, 2000: Evidence for enhanced mixing over rough topography in the abyssal  
964 ocean. *Nature*, **403** (6766), 179–182, doi:10.1038/35003164, URL [http://www.nature.](http://www.nature.com/articles/35003164)  
965 [com/articles/35003164](http://www.nature.com/articles/35003164), publisher: Nature Publishing Group.

966 Ledwell, J. R., A. J. Watson, and C. S. Law, 1993: Evidence for slow mixing across the pyc-  
967 nocline from an open-ocean tracer-release experiment. *Nature*, **364** (6439), 701–703, doi:  
968 10.1038/364701a0, URL <http://www.nature.com/doi/10.1038/364701a0>, publisher:  
969 Nature Publishing Group.

970 Legg, S., and Coauthors, 2009: Improving Oceanic Overflow Representation in Climate  
971 Models: The Gravity Current Entrainment Climate Process Team. *Bulletin of the*  
972 *American Meteorological Society*, **90** (5), 657–670, doi:10.1175/2008BAMS2667.1, URL  
973 [https://journals.ametsoc.org/view/journals/bams/90/5/2008bams2667\\_1.xml](https://journals.ametsoc.org/view/journals/bams/90/5/2008bams2667_1.xml), publisher:  
974 American Meteorological Society Section: Bulletin of the American Meteorological Soci-  
975 ety.

976 MacCready, P., and P. B. Rhines, 1991: Buoyant inhibition of Ekman transport on  
977 a slope and its effect on stratified spin-up. *Journal of Fluid Mechanics*, **223** (-1),

978 631, doi:10.1017/S0022112091001581, URL [http://www.journals.cambridge.org/abstract\\_](http://www.journals.cambridge.org/abstract_)  
979 S0022112091001581, publisher: Cambridge University Press.

980 Marshall, J., C. Hill, L. Perelman, and A. Adcroft, 1997: Hydrostatic, quasi-hydrostatic,  
981 and nonhydrostatic ocean modeling. *Journal of Geophysical Research*, **102 (C3)**, 5733,  
982 doi:10.1029/96JC02776, iISBN: 2156-2202.

983 Marshall, J., and T. Radko, 2003: Residual-Mean Solutions for the Antarctic Cir-  
984 cumpolar Current and Its Associated Overturning Circulation. *Journal of Physical*  
985 *Oceanography*, **33 (11)**, 2341–2354, doi:10.1175/1520-0485(2003)033<2341:RSFTAC>2.  
986 0.CO;2, URL [http://dx.doi.org/10.1175/1520-0485\(2003\)033%3C2341:RSFTAC%3E2.0](http://dx.doi.org/10.1175/1520-0485(2003)033%3C2341:RSFTAC%3E2.0).  
987 CO;2, iISBN: 0022-3670.

988 Mashayek, A., J. Gula, L. Baker, A. N. Garabato, L. Cimoli, and J. Riley, 2021: Mountains  
989 to climb: on the role of seamounts in upwelling of deep ocean water. Tech. rep. doi:10.  
990 21203/rs.3.rs-939198/v1, URL <https://doi.org/10.21203/rs.3.rs-939198/v1>, type: article.

991 McDougall, T. J., and R. Ferrari, 2017: Abyssal Upwelling and Downwelling Driven by  
992 Near-Boundary Mixing. *Journal of Physical Oceanography*, **47 (2)**, 261–283, doi:10.1175/  
993 JPO-D-16-0082.1, URL <https://journals.ametsoc.org/doi/full/10.1175/JPO-D-16-0082>.  
994 1, publisher: American Meteorological Society.

995 Melet, A., R. Hallberg, S. Legg, and M. Nikurashin, 2014: Sensitivity of the Ocean  
996 State to Lee Wave-Driven Mixing. *Journal of Physical Oceanography*, **44 (3)**, 900–  
997 921, doi:10.1175/JPO-D-13-072.1, URL <http://journals.ametsoc.org/doi/abs/10.1175/>  
998 JPO-D-13-072.1.

- 999 Morris, M. Y., M. M. Hall, L. C. S. Laurent, and N. G. Hogg, 2001: Abyssal Mixing in  
1000 the Brazil Basin. *Journal of Physical Oceanography*, **31** (11), 3331–3348, doi:10.1175/  
1001 1520-0485(2001)031<3331:AMITBB>2.0.CO;2, URL [https://journals.ametsoc.org/view/  
1002 journals/phoc/31/11/1520-0485\\_2001\\_031\\_3331\\_amitbb\\_2.0.co\\_2.xml](https://journals.ametsoc.org/view/journals/phoc/31/11/1520-0485_2001_031_3331_amitbb_2.0.co_2.xml), publisher: Ameri-  
1003 can Meteorological Society Section: Journal of Physical Oceanography.
- 1004 Munk, W. H., 1966: Abyssal recipes. *Deep Sea Research and Oceanographic Ab-*  
1005 *stracts*, **13** (4), 707–730, doi:10.1016/0011-7471(66)90602-4, arXiv: cs/9605103 ISBN:  
1006 1600117471.
- 1007 Naveira Garabato, A. C., and Coauthors, 2019: Rapid mixing and exchange of deep-ocean  
1008 waters in an abyssal boundary current. *Proceedings of the National Academy of Sci-*  
1009 *ences*, **116** (27), 13 233–13 238, doi:10.1073/pnas.1904087116, URL [https://www.pnas.  
1010 org/content/116/27/13233](https://www.pnas.org/content/116/27/13233), iISBN: 9781904087113 Publisher: National Academy of Sci-  
1011 ences Section: Physical Sciences.
- 1012 Nazarian, R. H., C. M. Burns, S. Legg, M. C. Buijsman, H. Kaur, and  
1013 B. K. Arbic, 2021: On the Magnitude of Canyon-Induced Mixing. *Jour-*  
1014 *nal of Geophysical Research: Oceans*, **126** (11), e2021JC017671, doi:10.1029/  
1015 2021JC017671, URL <https://onlinelibrary.wiley.com/doi/abs/10.1029/2021JC017671>,  
1016 \_eprint: <https://onlinelibrary.wiley.com/doi/pdf/10.1029/2021JC017671>.
- 1017 Nikurashin, M., and R. Ferrari, 2013: Overturning circulation driven by breaking internal  
1018 waves in the deep ocean. *Geophysical Research Letters*, **40** (12), 3133–3137, doi:10.1002/  
1019 grl.50542, URL <http://doi.wiley.com/10.1002/grl.50542>, publisher: Wiley-Blackwell.
- 1020 Nikurashin, M., and S. Legg, 2011: A Mechanism for Local Dissipation of Internal Tides Gen-  
1021 erated at Rough Topography. *Journal of Physical Oceanography*, **41** (2), 378–395, doi:10.

1022 1175/2010JPO4522.1, URL [http://journals.ametsoc.org/doi/abs/10.1175/2010JPO4522.](http://journals.ametsoc.org/doi/abs/10.1175/2010JPO4522.1)  
1023 1.

1024 Peterson, H. G., and J. Callies, 2021: Rapid spin up and spin down of flow along slopes.  
1025 *Journal of Physical Oceanography*, **-1 (aop)**, doi:10.1175/JPO-D-21-0173.1, URL [https://](https://journals.ametsoc.org/view/journals/phoc/aop/JPO-D-21-0173.1/JPO-D-21-0173.1.xml)  
1026 [journals.ametsoc.org/view/journals/phoc/aop/JPO-D-21-0173.1/JPO-D-21-0173.1.xml](https://journals.ametsoc.org/view/journals/phoc/aop/JPO-D-21-0173.1/JPO-D-21-0173.1.xml),  
1027 publisher: American Meteorological Society Section: Journal of Physical Oceanography.

1028 Phillips, O., 1970: On flows induced by diffusion in a stably stratified fluid. *Deep Sea Re-*  
1029 *search and Oceanographic Abstracts*, **17 (3)**, 435–443, doi:10.1016/0011-7471(70)90058-6,  
1030 URL <http://linkinghub.elsevier.com/retrieve/pii/0011747170900586>.

1031 Plumb, R. A., and R. Ferrari, 2005: Transformed Eulerian-Mean Theory. Part I: Nonquasi-  
1032 geostrophic Theory for Eddies on a Zonal-Mean Flow. *Journal of Physical Oceanography*,  
1033 **35 (2)**, 165–174, doi:10.1175/JPO-2669.1, URL [http://journals.ametsoc.org/doi/abs/10.](http://journals.ametsoc.org/doi/abs/10.1175/JPO-2669.1)  
1034 [1175/JPO-2669.1](http://journals.ametsoc.org/doi/abs/10.1175/JPO-2669.1).

1035 Polzin, K., J. Toole, J. R. Ledwell, and R. Schmitt, 1997: Spatial Variability of Tur-  
1036 bulent Mixing in the Spatial Variability Abyssal Ocean. *Science*, **276 (5309)**, 93–96,  
1037 doi:10.1126/science.276.5309.93, URL [http://www.sciencemag.org/cgi/content/abstract/](http://www.sciencemag.org/cgi/content/abstract/276/5309/93)  
1038 [276/5309/93](http://www.sciencemag.org/cgi/content/abstract/276/5309/93), iSBN: 0036-8075.

1039 Polzin, K. L., 2009: An abyssal recipe. *Ocean Modelling*, **30 (4)**, 298–309, doi:10.1016/j.  
1040 [ocemod.2009.07.006](https://doi.org/10.1016/j.ocemod.2009.07.006).

1041 Polzin, K. L., and T. J. McDougall, 2022: Chapter 7 - Mixing at the ocean’s bottom bound-  
1042 ary. *Ocean Mixing*, M. Meredith, and A. Naveira Garabato, Eds., Elsevier, 145–180,

1043 doi:10.1016/B978-0-12-821512-8.00014-1, URL [https://www.sciencedirect.com/science/](https://www.sciencedirect.com/science/article/pii/B9780128215128000141)  
1044 [article/pii/B9780128215128000141](https://www.sciencedirect.com/science/article/pii/B9780128215128000141).

1045 Polzin, K. L., B. Wang, Z. Wang, F. Thwaites, and A. J. Williams, 2021: Moored Flux and  
1046 Dissipation Estimates from the Northern Deepwater Gulf of Mexico. *Fluids*, **6 (7)**, 237,  
1047 doi:10.3390/fluids6070237, URL <https://www.mdpi.com/2311-5521/6/7/237>, number: 7  
1048 Publisher: Multidisciplinary Digital Publishing Institute.

1049 Pratt, L., and J. Whitehead, 2008: *Rotating Hydraulics: Nonlinear Topographic Effects in*  
1050 *the Ocean and Atmosphere*.

1051 Rhines, P. B., and W. R. Young, 1982: Homogenization of potential vorticity in planetary  
1052 gyres. *Journal of Fluid Mechanics*, **122 (-1)**, 347, doi:10.1017/S0022112082002250, URL  
1053 [http://www.journals.cambridge.org/abstract\\_S0022112082002250](http://www.journals.cambridge.org/abstract_S0022112082002250).

1054 Ruan, X., and J. Callies, 2020: Mixing-Driven Mean Flows and Submesoscale Eddies over  
1055 Mid-Ocean Ridge Flanks and Fracture Zone Canyons. *Journal of Physical Oceanogra-*  
1056 *phy*, **50 (1)**, 175–195, doi:10.1175/JPO-D-19-0174.1, URL [https://journals.ametsoc.org/](https://journals.ametsoc.org/view/journals/phoc/50/1/jpo-d-19-0174.1.xml)  
1057 [view/journals/phoc/50/1/jpo-d-19-0174.1.xml](https://journals.ametsoc.org/view/journals/phoc/50/1/jpo-d-19-0174.1.xml), publisher: American Meteorological Soci-  
1058 ety Section: Journal of Physical Oceanography.

1059 Salmun, H., P. D. Killworth, and J. R. Blundell, 1991: A two-dimensional model of boundary  
1060 mixing. *Journal of Geophysical Research: Oceans*, **96 (C10)**, 18 447–18 474, doi:10.1029/  
1061 91JC01917, URL <https://agupubs.onlinelibrary.wiley.com/doi/abs/10.1029/91JC01917>.

1062 Smith, W. H. F., and D. T. Sandwell, 1997: Global Sea Floor Topography from Satel-  
1063 lite Altimetry and Ship Depth Soundings. *Science*, **277 (5334)**, 1956–1962, doi:10.1126/

1064 science.277.5334.1956, URL <https://science.sciencemag.org/content/277/5334/1956>, pub-  
1065 lisher: American Association for the Advancement of Science Section: Research Article.

1066 Spingys, C. P., A. C. N. Garabato, S. Legg, K. L. Polzin, E. P. Abrahamson, C. E. Buck-  
1067 ingham, A. Forryan, and E. E. Frajka-Williams, 2021: Mixing and Transformation in  
1068 a Deep Western Boundary Current: A Case Study. *Journal of Physical Oceanography*,  
1069 **51** (4), 1205–1222, doi:10.1175/JPO-D-20-0132.1, URL [https://journals.ametsoc.org/  
1070 view/journals/phoc/aop/JPO-D-20-0132.1/JPO-D-20-0132.1.xml](https://journals.ametsoc.org/view/journals/phoc/aop/JPO-D-20-0132.1/JPO-D-20-0132.1.xml), publisher: American  
1071 Meteorological Society Section: Journal of Physical Oceanography.

1072 St. Laurent, L., and C. Garrett, 2002: The Role of Internal Tides in Mixing the  
1073 Deep Ocean. *Journal of Physical Oceanography*, **32** (10), 2882–2899, doi:10.1175/  
1074 1520-0485(2002)032<2882:TROITI>2.0.CO;2, URL [http://journals.ametsoc.org/doi/abs/  
1075 10.1175/1520-0485%282002%29032%3C2882%3ATROITI%3E2.0.CO%3B2](http://journals.ametsoc.org/doi/abs/10.1175/1520-0485%282002%29032%3C2882%3ATROITI%3E2.0.CO%3B2).

1076 St. Laurent, L. C., J. M. Toole, and R. W. Schmitt, 2001: Buoyancy Forcing by Turbulence  
1077 above Rough Topography in the Abyssal Brazil Basin\*. *Journal of Physical Oceanography*,  
1078 **31** (12), 3476–3495, doi:10.1175/1520-0485(2001)031<3476:BFBTAR>2.0.CO;2.

1079 Stommel, H., 1958: The abyssal circulation. *Deep Sea Research (1953)*, **5** (1), 80–  
1080 82, doi:10.1016/S0146-6291(58)80014-4, URL [https://www.sciencedirect.com/science/  
1081 article/pii/S0146629158800144](https://www.sciencedirect.com/science/article/pii/S0146629158800144).

1082 Stone, P. H., 1966: On Non-Geostrophic Baroclinic Stability. *Journal of the Atmo-  
1083 spheric Sciences*, **23** (4), 390–400, doi:10.1175/1520-0469(1966)023<0390:ONGBS>2.0.  
1084 CO;2, URL [https://journals.ametsoc.org/view/journals/atsc/23/4/1520-0469\\_1966\\_023\\_  
1085 0390\\_ongbs\\_2\\_0\\_co\\_2.xml](https://journals.ametsoc.org/view/journals/atsc/23/4/1520-0469_1966_023_0390_ongbs_2_0_co_2.xml), publisher: American Meteorological Society Section: Journal  
1086 of the Atmospheric Sciences.

- 1087 Sverdrup, H., M. Johnson, and R. Fleming, 1942: The Oceans: Their Physics, Chemistry  
1088 and General Biology. *Oceanography*, 1104, doi:10.2307/210609, arXiv: 1011.1669v3 ISBN:  
1089 9788578110796.
- 1090 Talley, L. D., 2013: Closure of the Global Overturning Circulation Through the Indian,  
1091 Pacific, and Southern Oceans: Schematics and Transports. *Oceanography*, **26 (1)**, 80–97,  
1092 doi:10.5670/oceanog.2013.07, URL [http://apps.webofknowledge.com/full\\_record.do?](http://apps.webofknowledge.com/full_record.do?product=UA&search_mode=GeneralSearch&qid=14&SID=W1jPgX8kkS6brME6NvD&page=1&doc=1)  
1093 [product=UA&search\\_mode=GeneralSearch&qid=14&SID=W1jPgX8kkS6brME6NvD&](http://apps.webofknowledge.com/full_record.do?product=UA&search_mode=GeneralSearch&qid=14&SID=W1jPgX8kkS6brME6NvD&page=1&doc=1)  
1094 [page=1&doc=1](http://apps.webofknowledge.com/full_record.do?product=UA&search_mode=GeneralSearch&qid=14&SID=W1jPgX8kkS6brME6NvD&page=1&doc=1), arXiv: 1011.1669v3 ISBN: 1042-8275.
- 1095 Talley, L. D., J. L. Reid, and P. E. Robbins, 2003: Data-Based Meridional Overturning  
1096 Streamfunctions for the Global Ocean. *Journal of Climate*, **16 (19)**, 3213–3226, doi:  
1097 10.1175/1520-0442(2003)016<3213:DMOSFT>2.0.CO;2, URL [https://journals.ametsoc.](https://journals.ametsoc.org/view/journals/clim/16/19/1520-0442.2003_016_3213_dmosft_2.0.co_2.xml)  
1098 [org/view/journals/clim/16/19/1520-0442.2003\\_016\\_3213\\_dmosft\\_2.0.co\\_2.xml](https://journals.ametsoc.org/view/journals/clim/16/19/1520-0442.2003_016_3213_dmosft_2.0.co_2.xml), publisher:  
1099 American Meteorological Society Section: Journal of Climate.
- 1100 Taylor, G. I., and W. N. Shaw, 1920: I. Tidal friction in the Irish Sea. *Philosophical*  
1101 *Transactions of the Royal Society of London. Series A, Containing Papers of a Math-*  
1102 *ematical or Physical Character*, **220 (571-581)**, 1–33, doi:10.1098/rsta.1920.0001, URL  
1103 <https://royalsocietypublishing.org/doi/10.1098/rsta.1920.0001>, publisher: Royal Society.
- 1104 Thompson, L., and G. C. Johnson, 1996: Abyssal currents generated by diffusion and  
1105 geothermal heating over rises. *Deep Sea Research Part I: Oceanographic Research Pa-*  
1106 *pers*, **43 (2)**, 193–211, doi:10.1016/0967-0637(96)00095-7, URL [http://www.sciencedirect.](http://www.sciencedirect.com/science/article/pii/0967063796000957)  
1107 [com/science/article/pii/0967063796000957](http://www.sciencedirect.com/science/article/pii/0967063796000957).
- 1108 Thorpe, S. A., 1987: Current and Temperature Variability on the Continental Slope.  
1109 *Philosophical Transactions of the Royal Society A: Mathematical, Physical and Engi-*

- 1110 *neering Sciences*, **323** (1574), 471–517, doi:10.1098/rsta.1987.0100, URL <http://rsta.royalsocietypublishing.org/cgi/doi/10.1098/rsta.1987.0100>, publisher: The Royal Society.
- 1111
- 1112 Thorpe, S. A., 2005: *The Turbulent Ocean*. Cambridge University Press, Cam-  
1113 bridge, doi:10.1017/CBO9780511819933, URL <https://www.cambridge.org/core/books/turbulent-ocean/1F9A34350F4AA077CA27641C6884B61B>.
- 1114
- 1115 Thurnherr, A. M., 2000: Hydrography and flow in the rift valley of the Mid-Atlantic Ridge.  
1116 phd, University of Southampton, URL <https://eprints.soton.ac.uk/42174/>.
- 1117 Thurnherr, A. M., L. Clément, L. S. Laurent, R. Ferrari, and T. Ijichi, 2020: Transformation  
1118 and Upwelling of Bottom Water in Fracture Zone Valleys. *Journal of Physical Oceanog-*  
1119 *raphy*, **50** (3), 715–726, doi:10.1175/JPO-D-19-0021.1, URL <https://journals.ametsoc.org/view/journals/phoc/50/3/jpo-d-19-0021.1.xml>, publisher: American Meteorological  
1120 Society Section: Journal of Physical Oceanography.
- 1121
- 1122 Thurnherr, A. M., and K. G. Speer, 2003: Boundary Mixing and Topographic  
1123 Blocking on the Mid-Atlantic Ridge in the South Atlantic\*. *Journal of Physi-*  
1124 *cal Oceanography*, **33** (4), 848–862, doi:10.1175/1520-0485(2003)33<848:BMATBO>2.  
1125 0.CO;2, URL <http://journals.ametsoc.org/doi/abs/10.1175/1520-0485%282003%2933%3C848%3ABMATBO%3E2.0.CO%3B2>.
- 1126
- 1127 Thurnherr, A. M., and Coauthors, 2005: Mixing Associated with Sills in a Canyon on  
1128 the Midocean Ridge Flank\*. *Journal of Physical Oceanography*, **35** (8), 1370–1381, doi:  
1129 10.1175/JPO2773.1, URL <http://journals.ametsoc.org/doi/abs/10.1175/JPO2773.1>.
- 1130 Toole, J. M., 2007: Temporal Characteristics of Abyssal Finescale Motions above Rough  
1131 Bathymetry. *Journal of Physical Oceanography*, **37** (3), 409–427, doi:10.1175/JPO2988.

1, URL <https://journals.ametsoc.org/view/journals/phoc/37/3/jpo2988.1.xml>, publisher:  
American Meteorological Society Section: Journal of Physical Oceanography.

Tozer, B., D. T. Sandwell, W. H. F. Smith, C. Olson, J. R. Beale, and P. Wes-  
sel, 2019: Global Bathymetry and Topography at 15 Arc Sec: SRTM15+.  
*Earth and Space Science*, **6** (10), 1847–1864, doi:10.1029/2019EA000658, URL  
<https://agupubs.onlinelibrary.wiley.com/doi/abs/10.1029/2019EA000658>, eprint:  
<https://agupubs.onlinelibrary.wiley.com/doi/pdf/10.1029/2019EA000658>.

Tziperman, E., 1986: On the Role of Interior Mixing and Air-Sea Fluxes in De-  
termining the Stratification and Circulation of the Oceans. *Journal of Physical  
Oceanography*, **16** (4), 680–693, doi:10.1175/1520-0485(1986)016<0680:OTROIM>2.0.  
CO;2, URL [https://journals.ametsoc.org/view/journals/phoc/16/4/1520-0485\\_1986\\_016\\_0680\\_otroim\\_2\\_0\\_co\\_2.xml](https://journals.ametsoc.org/view/journals/phoc/16/4/1520-0485_1986_016_0680_otroim_2_0_co_2.xml), publisher: American Meteorological Society Section: Journal  
of Physical Oceanography.

van Haren, H., 2018: High-Resolution Observations of Internal Wave Turbulence in the  
Deep Ocean. *The Ocean in Motion: Circulation, Waves, Polar Oceanography*, M. G.  
Velarde, R. Y. Tarakanov, and A. V. Marchenko, Eds., Springer Oceanography, Springer  
International Publishing, Cham, 127–146, doi:10.1007/978-3-319-71934-4\_11, URL [https://doi.org/10.1007/978-3-319-71934-4\\_11](https://doi.org/10.1007/978-3-319-71934-4_11).

Voet, G., J. B. Girton, M. H. Alford, G. S. Carter, J. M. Klymak, and J. B. Mickett,  
2015: Pathways, Volume Transport, and Mixing of Abyssal Water in the Samoan Pas-  
sage. *Journal of Physical Oceanography*, **45** (2), 562–588, doi:10.1175/JPO-D-14-0096.1,  
URL <https://journals.ametsoc.org/view/journals/phoc/45/2/jpo-d-14-0096.1.xml>, pub-  
lisher: American Meteorological Society Section: Journal of Physical Oceanography.

- 1155 Walin, G., 1982: On the relation between sea-surface heat flow and thermal circulation in  
1156 the ocean. *Tellus*, **34** (2), 187–195, doi:10.3402/tellusa.v34i2.10801, URL [https://doi.org/  
1157 10.3402/tellusa.v34i2.10801](https://doi.org/10.3402/tellusa.v34i2.10801).
- 1158 Watson, A. J., J. R. Ledwell, D. J. Webb, and C. Wunsch, 1988: Purposefully Released  
1159 Tracers [and Discussion]. *Philosophical Transactions of the Royal Society of London. Series  
1160 A, Mathematical and Physical Sciences*, **325** (1583), 189–200, URL [https://www.jstor.  
1161 org/stable/38109](https://www.jstor.org/stable/38109), publisher: The Royal Society.
- 1162 Wenegrat, J. O., J. Callies, and L. N. Thomas, 2018: Submesoscale Baroclinic Insta-  
1163 bility in the Bottom Boundary Layer. *Journal of Physical Oceanography*, JPO–D–17–  
1164 0264.1, doi:10.1175/JPO-D-17-0264.1, URL [http://journals.ametsoc.org/doi/10.1175/  
1165 JPO-D-17-0264.1](http://journals.ametsoc.org/doi/10.1175/JPO-D-17-0264.1).
- 1166 Whalen, C. B., 2021: Best Practices for Comparing Ocean Turbulence Measurements across  
1167 Spatiotemporal Scales. *Journal of Atmospheric and Oceanic Technology*, **38** (4), 837–  
1168 841, doi:10.1175/JTECH-D-20-0175.1, URL [https://journals.ametsoc.org/view/journals/  
1169 atot/38/4/JTECH-D-20-0175.1.xml](https://journals.ametsoc.org/view/journals/atot/38/4/JTECH-D-20-0175.1.xml), publisher: American Meteorological Society Section:  
1170 Journal of Atmospheric and Oceanic Technology.
- 1171 Whalen, C. B., C. de Lavergne, A. C. Naveira Garabato, J. M. Klymak, J. A. MacKinnon,  
1172 and K. L. Sheen, 2020: Internal wave-driven mixing: governing processes and conse-  
1173 quences for climate. *Nature Reviews Earth & Environment*, **1** (11), 606–621, doi:10.1038/  
1174 s43017-020-0097-z, URL <https://www.nature.com/articles/s43017-020-0097-z>, number:  
1175 11 Publisher: Nature Publishing Group.
- 1176 Winters, K. B., and L. Armi, 2012: Hydraulic control of continuously stratified flow over  
1177 an obstacle. *Journal of Fluid Mechanics*, **700**, 502–513, doi:10.1017/jfm.2012.157,

1178 URL [https://www.cambridge.org/core/journals/journal-of-fluid-mechanics/](https://www.cambridge.org/core/journals/journal-of-fluid-mechanics/article/abs/hydraulic-control-of-continuously-stratified-flow-over-an-obstacle/0A67346BF37CCAE5EFACC92238FD92CA)  
1179 [article/abs/hydraulic-control-of-continuously-stratified-flow-over-an-obstacle/](https://www.cambridge.org/core/journals/journal-of-fluid-mechanics/article/abs/hydraulic-control-of-continuously-stratified-flow-over-an-obstacle/0A67346BF37CCAE5EFACC92238FD92CA)  
1180 [0A67346BF37CCAE5EFACC92238FD92CA](https://www.cambridge.org/core/journals/journal-of-fluid-mechanics/article/abs/hydraulic-control-of-continuously-stratified-flow-over-an-obstacle/0A67346BF37CCAE5EFACC92238FD92CA), publisher: Cambridge University Press.

1181 Wunsch, C., 1970: On oceanic boundary mixing. *Deep-Sea Research and Oceanographic*  
1182 *Abstracts*, **17** (2), 293–301, doi:10.1016/0011-7471(70)90022-7.

1183 Young, W. R., 2011: An Exact Thickness-Weighted Average Formulation of the Boussi-  
1184 nesq Equations. *Journal of Physical Oceanography*, **42** (5), 692–707, doi:10.1175/  
1185 JPO-D-11-0102.1, URL [https://journals.ametsoc.org/doi/full/10.1175/JPO-D-11-0102.](https://journals.ametsoc.org/doi/full/10.1175/JPO-D-11-0102.1)  
1186 1.

1187 **LIST OF FIGURES**

1188 **Fig. 1.** Height above bottom stratification profiles at steady state for 1D BBL models:  
 1189 with the same external parameters as the BBTRE simulations (solid), without  
 1190 rotation ( $f = 0$ ; dotted), and with enhanced vertical diffusion of along-slope  
 1191 momentum,  $\sigma_v(z) \gg 1$  (dash-dotted; see Appendix). . . . . 61

1192 **Fig. 2.** A generalized slope-normal buoyancy budget (16), derived by integrating the  
 1193 buoyancy equation below a given height above the mean slope  $z$  (volume shown  
 1194 in light blue); at equilibrium, the mean up-slope transport (across the background  
 1195 stratification  $N^2$ ) into the box (blue lines) is given by the net flux of buoyancy  
 1196 into the box from above (red line),  $\Psi \propto -\langle -\kappa B_z \rangle - \langle wb \rangle$ . We assume no buoyancy  
 1197 flux across the seafloor (black line) at  $z = \max(d) - d(x, y)$ . . . . . 62

1198 **Fig. 3.** Numerical model domains. (a) Seafloor elevation  $-\hat{d}(\hat{x}, \hat{y})$ , including the doubly-  
 1199 periodic simulation domain centered on the Brazil Basin Tracer Release Exper-  
 1200 iment (BBTRE) canyon. Red markers show the locations of moorings from  
 1201 Clément et al. (2017) (CTS17) and Thurnherr et al. (2005) (T05). The inset  
 1202 highlights the DoMORE sill that dramatically constrains up-canyon flow. White  
 1203 markers mark the injection location from the BBTRE (Ledwell et al. 2000). (b)  
 1204 Imposed slope-normal diffusivity field, the result of applying a self-similar ex-  
 1205 ponential profile as a function of the height-above-bottom (eq. 17) to variable  
 1206 topography. Arrows show the original along-canyon  $\hat{y}$  and cross-canyon  $\hat{x}$  direc-  
 1207 tions as well as the transformed slope-normal  $\mathbf{z}$  and along-canyon  $\mathbf{x}$  coordinate  
 1208 vectors (a), which appear distorted because the vertical dimension is exagger-  
 1209 ated (b). (c-f) A hierarchy of simulations with progressively complex seafloor  
 1210 bathymetry geometries (relative to a constant mean slope of angle  $\theta$ ; see dashed  
 1211 lines in panel b). Thin black lines distinguish three sub-regions: the canyon  
 1212 trough, the canyon’s flanks, and the ridge flank surrounding the canyon. . . . . 63

1213 **Fig. 4.** Structure of up-canyon mean flow in the BBTRE Canyon. (a) Along-canyon-  
 1214 averaged up-canyon flow  $\bar{u}^x$ , with the mean canyon seafloor outlined in trans-  
 1215 parent grey shading and cross-canyon thalweg shown in the dark gray shading.  
 1216 (b) Cross-canyon-averaged up-canyon flow  $\bar{u}^y$  in the original coordinate frame  
 1217 ( $\hat{x}, \hat{z}$ ). Grey lines represent equally-spaced buoyancy surfaces. The much gentler  
 1218 isopycnal slopes seen in some hydrographic sections of canyons, as in Thurnherr  
 1219 et al. 2020, are largely an artifact of their much lower horizontal resolution, as  
 1220 evidenced by the favorable comparison in Figure 6. The black line marks the  
 1221 mean seafloor depth of the half of the domain furthest from the canyon thalweg  
 1222 and acts as a proxy for the crest of the canyon. (c) Up-canyon flux, integrated  
 1223 in the slope-normal direction  $z$ . Black and grey contours show a deep and shal-  
 1224 low isobath, respectively, to highlight the canyon topography that shallows to  
 1225 the right. (d) Same as (c), but integrated only from  $z = 0$  m to  $z = 800$  m to  
 1226 highlight the core up-canyon jet within the canyon. . . . . 64

1227 **Fig. 5.** Structure of up-canyon flow at two mooring sites. (a,c) Cross-canyon sections  
 1228 of the up-canyon flow at the locations of the DoMORE sill mooring (Clément  
 1229 et al. 2017) (CTS17-P1) and the BBTRE mooring Thurnherr et al. (2005) (T05).  
 1230 Light grey shading shows the local seafloor depth while the dark grey shading in  
 1231 (a) shows the mean height of the canyon floor above the mean slope, highlighting  
 1232 the significant vertical and cross-canyon constriction introduced by the sill. (b,d)  
 1233 Height-above-bottom profiles of the up-canyon flow at the locations of the two  
 1234 moorings (light grey lines) and shifted a few grid columns over to improve capture

1235 the core of the jet (black lines), which is somewhat displaced due to the coarse  
 1236 model bathymetry. . . . . 65

1237 **Fig. 6.** Comparison between observed and simulated stratification in the BBTRE Canyon  
 1238 region. (a) Height above bottom-averaged profile of stratification for the full  
 1239 simulation domain (solid blue), for the sample-mean of nine co-located CTD casts  
 1240 (dotted red; Ledwell et al. 2000), free-falling HRP-microstructure profiles (dashed  
 1241 red; Polzin et al. 1997), and simulated CTD casts (solid red). The dashed blue  
 1242 line shows the sample-mean of 10 HRP profiles that follow the canyon crest just  
 1243 north of the domain. (b) Observed (solid) and simulated (dashed) density profiles  
 1244 at the nine locations sampled by the BBTRE observational campaign, overlaid  
 1245 on a map of the seafloor-elevation. An additional simulated profile typical of the  
 1246 crest region outside of the canyon is also shown, revealing an apparent sampling  
 1247 bias due to the strategy of measuring weakly-stratified deep depressions along  
 1248 the trough of the canyon in search of the released tracer (Ledwell et al. 2000). . . . . 66

1249 **Fig. 7.** Instantaneous normalized relative vorticity  $\zeta/f$ , or local Rossby number, in and  
 1250 above the BBTRE Canyon at four different heights above the mean slope, at  
 1251  $t = 5050$  days. . . . . 67

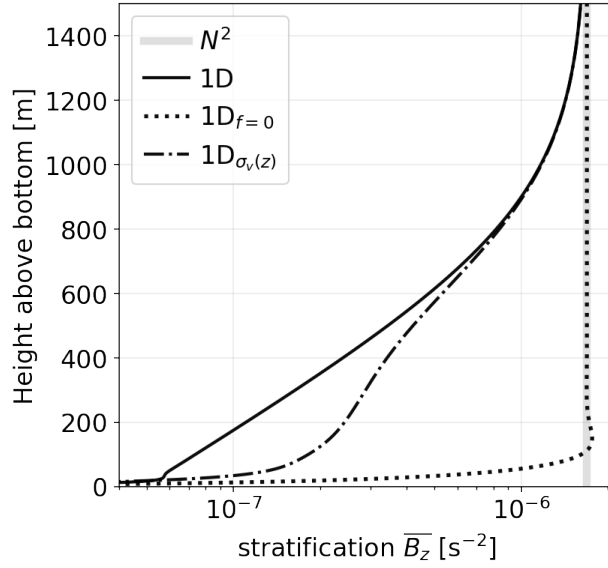
1252 **Fig. 8.** Generalized integral buoyancy budget in a hierarchy of increasingly complex simu-  
 1253 lations of mixing-driven flows up a mean slope of angle  $\theta$ : (a) 1D, (b) Smooth3D,  
 1254 (c)  $1D_{\sigma_v(z)}$ , (d) Canyon, (e) Canyon+Sill, (f) BBTRE. Solid lines show terms  
 1255 of the volume-integrated buoyancy budget (eq. 16), averaged over days 5000 to  
 1256 5200, for a layer bounded by a given Height Above the Mean Slope (HAMS).  
 1257 We interpret the sum of the Mean Flow and Eddy terms as a Residual Flow.  
 1258 The left-hand-side tendencies (LHS) are equal to the remainder of the approx-  
 1259 imate balance (RHS) between slope-normal turbulent diffusion and the cross-  
 1260 slope residual circulation, which includes both mean and eddy components. We  
 1261 divide (eq. 16) by the factor  $N^2 L_x \sin \theta$  to conveniently express the budget in  
 1262 terms of the quantity of interest, the up-slope volume transport  $\Psi$  with units of  
 1263  $mSv \equiv 10^3 m^3/s$ . Dotted lines in (a,c) show 1D steady state solutions and the  
 1264 dashed red line shows the integral constraint (eq. 13); in panels a and b, some of  
 1265 the dotted lines appear missing because they overlap with others. Grey shading  
 1266 shows the HAMS range spanned by the canyon, if present. . . . . 68

1267 **Fig. 9.** Height above bottom-averaged stratification profiles at  $t = 5000$  days, as a func-  
 1268 tion of model complexity (lines) and domain sub-region (panels b & c). Panel  
 1269 (a) and grey lines in (b,c) show one-dimensional solutions: with the same param-  
 1270 eters as the BBTRE simulations (solid); without a mean-slope ( $\theta = 0$ ; dashed),  
 1271 without rotation ( $f = 0$ ; dotted); and with an enhanced along-slope turbulent  
 1272 Prandtl number  $\sigma_v(z)$ , a crude proxy for restratification by submesoscale baro-  
 1273 clinic eddies (dash-dotted). Colored lines show a hierarchy of three-dimensional  
 1274 simulations with increasingly complex topographies (see Figure 3c-f). Arrows  
 1275 show how the stratification profiles evolve when processes are added: 1. adding  
 1276 a mean-slope, 2. allowing three-dimensional eddies, 3. introducing a cross-slope  
 1277 canyon, 4. blocking the canyon with a sill, and 5. adding realistic hills (i.e., the  
 1278 BBTRE topography). . . . . 69

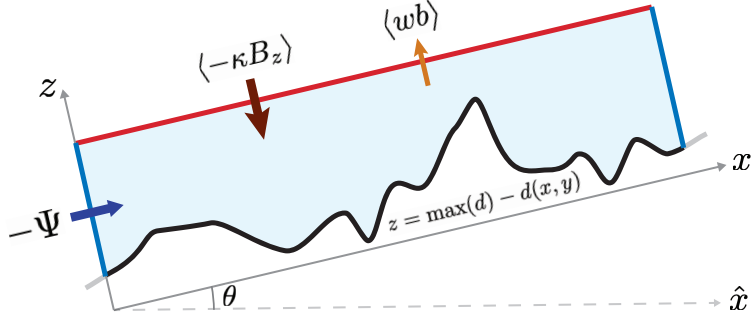
1279 **Fig. 10.** Cross-slope (left) and along-slope (right) sections of the stratification along the  
 1280 trough of a canyon in a hierarchy of numerical simulations (Smooth3D has no  
 1281 canyon, so the section is arbitrary). Solid grey lines in the left column show  
 1282 the approximate elevation of the ridge flanks surrounding the canyon while in

1283 the right column they show HAMS of the topographic sill (if present). Dashed  
 1284 grey lines show the locations of the respective sections. Black lines in panel (d)  
 1285 represent equally-spaced buoyancy surfaces. . . . . 70

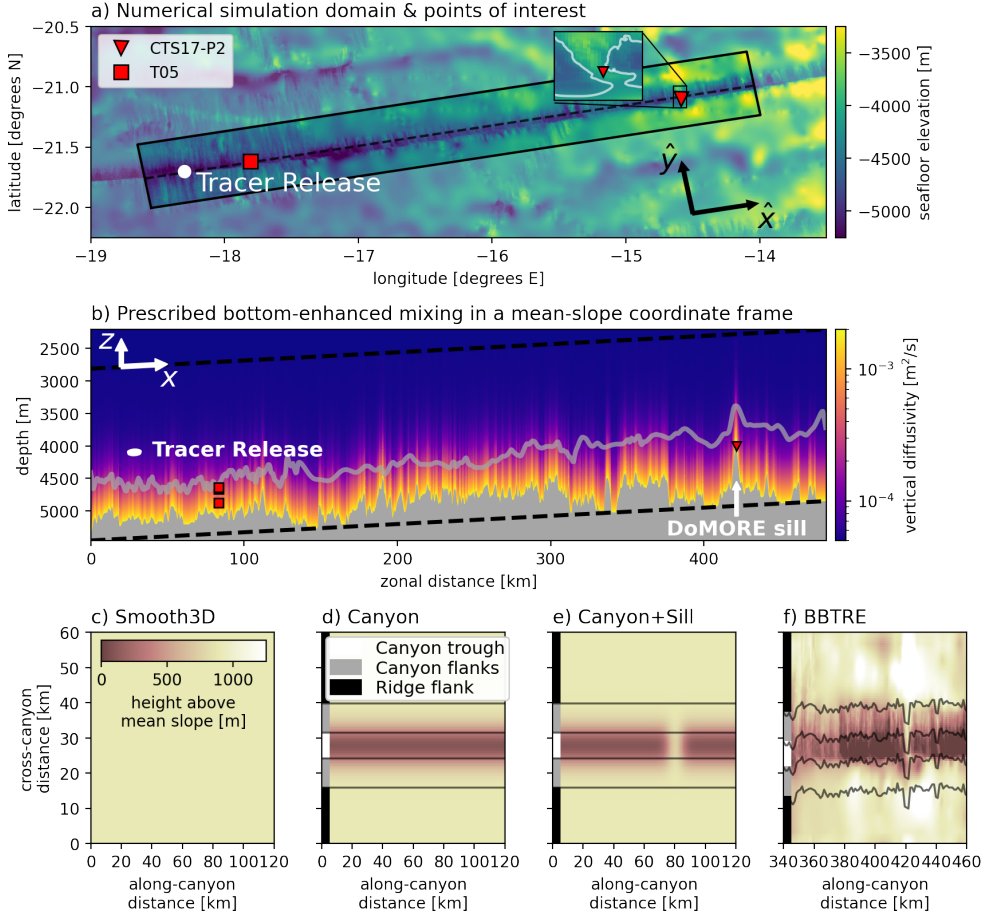
1286 **Fig. 11.**a) An idealized  $\sigma_v(z)$  profile (dash-dotted) with vertical scale  $\eta = 225$  m, tuned  
 1287 to the Smooth3D model that resolves submesoscale baroclinic instabilities us-  
 1288 ing equation (A12; solid blue). b) The ratio of the mean isopycnal slope  
 1289  $s_b = -N^2 \sin \theta / (N^2 \cos \theta + \bar{b}_z)$  to the horizontally-averaged eddy flux slope  
 1290  $s = \frac{w'b'}{u'b'}$ , which is  $\mathcal{O}(1)$  outside of the strongly diabatic and frictional bottom  
 1291 layer. The discontinuity near 750 m is due sign reversals in both the perturba-  
 1292 tion stratification and the slope-normal eddy buoyancy flux, which enter in the  
 1293 denominators of expressions for  $\sigma_v$  and  $s^{-1}$ , respectively. . . . . 71



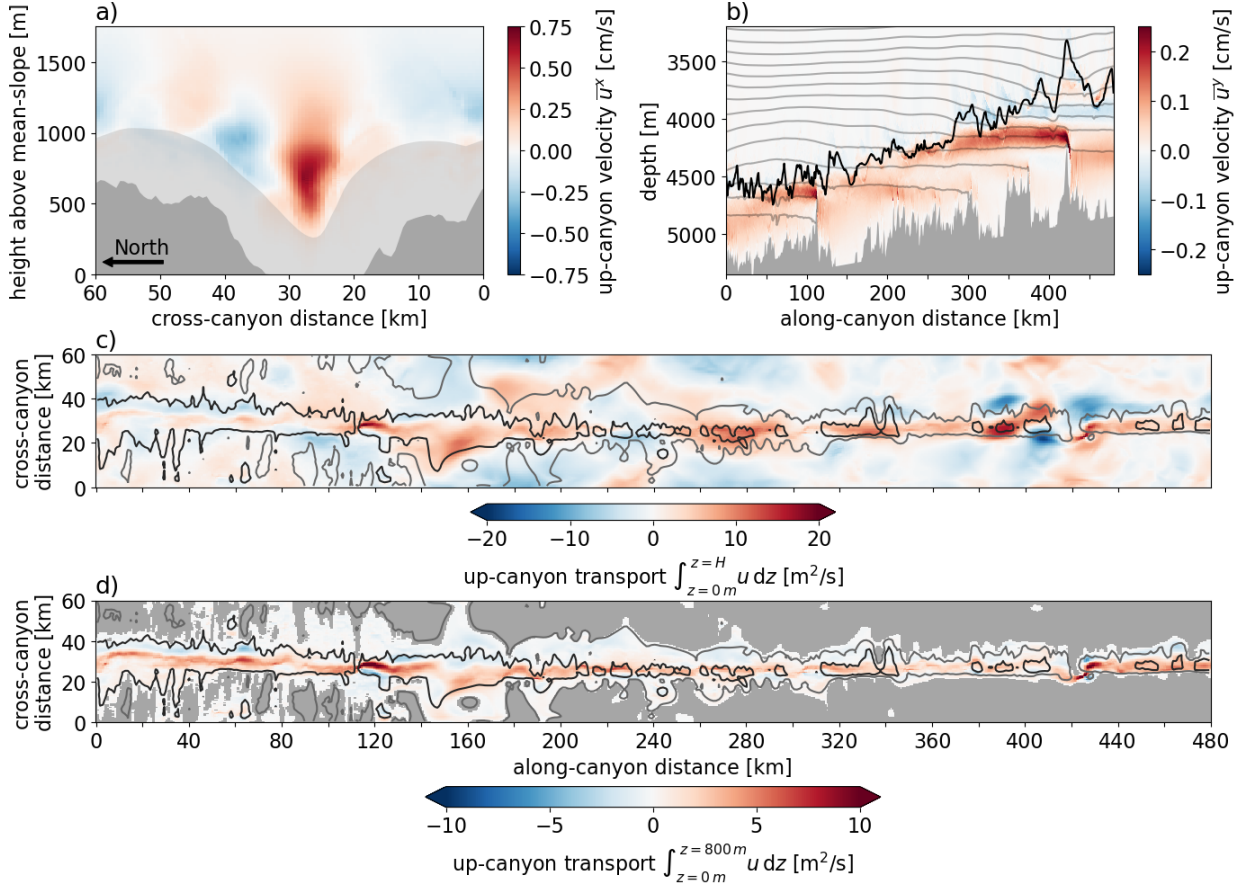
1294 FIG. 1. Height above bottom stratification profiles at steady state for 1D BBL models: with the  
 1295 same external parameters as the BBTRE simulations (solid), without rotation ( $f = 0$ ; dotted), and  
 1296 with enhanced vertical diffusion of along-slope momentum,  $\sigma_v(z) \gg 1$  (dash-dotted; see Appendix).



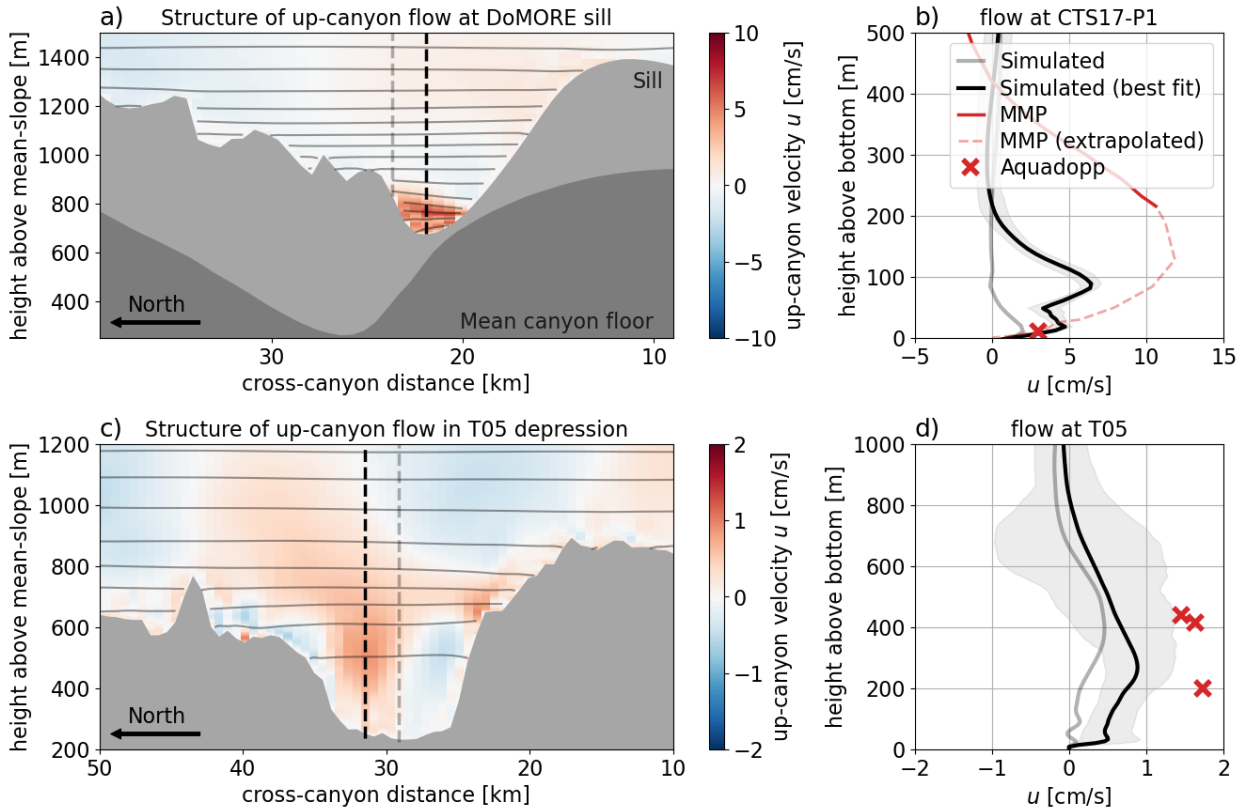
1297 FIG. 2. A generalized slope-normal buoyancy budget (16), derived by integrating the buoyancy  
 1298 equation below a given height above the mean slope  $z$  (volume shown in light blue); at equilibrium,  
 1299 the mean up-slope transport (across the background stratification  $N^2$ ) into the box (blue lines) is  
 1300 given by the net flux of buoyancy into the box from above (red line),  $\Psi \propto -\langle -\kappa B_z \rangle - \langle wb \rangle$ . We  
 1301 assume no buoyancy flux across the seafloor (black line) at  $z = \max(d) - d(x, y)$ .



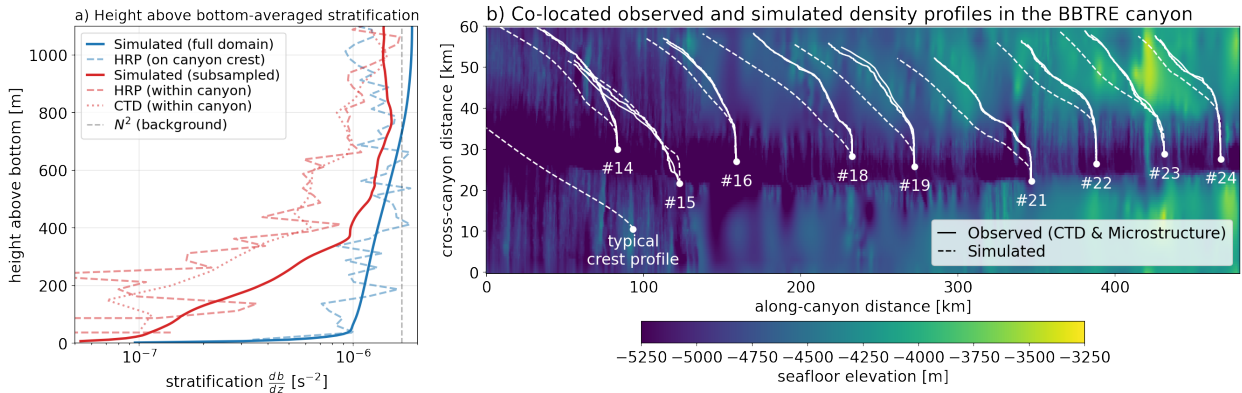
1302 FIG. 3. Numerical model domains. (a) Seafloor elevation  $-\hat{d}(\hat{x}, \hat{y})$ , including the doubly-periodic  
 1303 simulation domain centered on the Brazil Basin Tracer Release Experiment (BBTRE) canyon. Red  
 1304 markers show the locations of moorings from Clément et al. (2017) (CTS17) and Thurnherr et al.  
 1305 (2005) (T05). The inset highlights the DoMORE sill that dramatically constrains up-canyon flow.  
 1306 White markers mark the injection location from the BBTRE (Ledwell et al. 2000). (b) Imposed  
 1307 slope-normal diffusivity field, the result of applying a self-similar exponential profile as a function of  
 1308 the height-above-bottom (eq. 17) to variable topography. Arrows show the original along-canyon  
 1309  $\hat{y}$  and cross-canyon  $\hat{x}$  directions as well as the transformed slope-normal  $\mathbf{z}$  and along-canyon  $\mathbf{x}$   
 1310 coordinate vectors (a), which appear distorted because the vertical dimension is exaggerated (b).  
 1311 (c-f) A hierarchy of simulations with progressively complex seafloor bathymetry geometries (relative  
 1312 to a constant mean slope of angle  $\theta$ ; see dashed lines in panel b). Thin black lines distinguish three  
 1313 sub-regions: the canyon trough, the canyon's flanks, and the ridge flank surrounding the canyon.



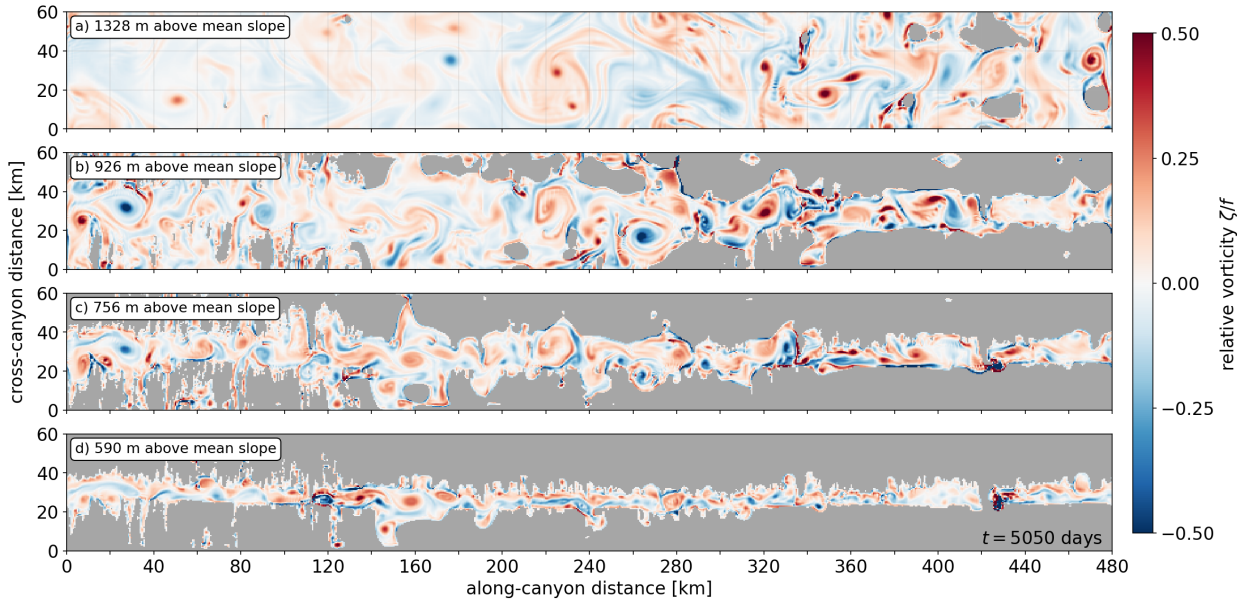
1314 FIG. 4. Structure of up-canyon mean flow in the BBTRE Canyon. (a) Along-canyon-averaged  
 1315 up-canyon flow  $\bar{u}^x$ , with the mean canyon seafloor outlined in transparent grey shading and cross-  
 1316 canyon thalweg shown in the dark gray shading. (b) Cross-canyon-averaged up-canyon flow  $\bar{u}^y$   
 1317 in the original coordinate frame  $(\hat{x}, \hat{z})$ . Grey lines represent equally-spaced buoyancy surfaces. The  
 1318 much gentler isopycnal slopes seen in some hydrographic sections of canyons, as in Thurnherr et al.  
 1319 2020, are largely an artifact of their much lower horizontal resolution, as evidenced by the favorable  
 1320 comparison in Figure 6. The black line marks the mean seafloor depth of the half of the domain  
 1321 furthest from the canyon thalweg and acts as a proxy for the crest of the canyon. (c) Up-canyon  
 1322 flux, integrated in the slope-normal direction  $z$ . Black and grey contours show a deep and shallow  
 1323 isobath, respectively, to highlight the canyon topography that shallows to the right. (d) Same as  
 1324 (c), but integrated only from  $z = 0$  m to  $z = 800$  m to highlight the core up-canyon jet within the  
 1325 canyon.



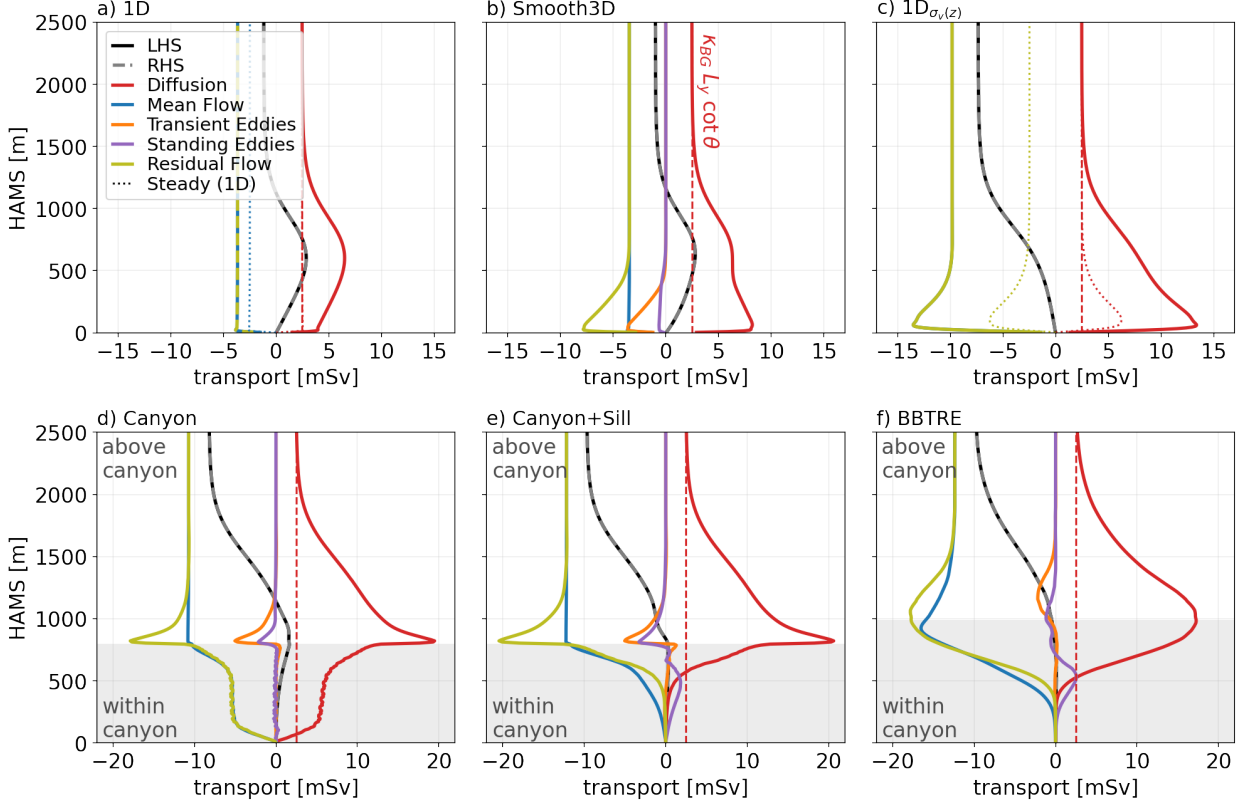
1326 FIG. 5. Structure of up-canyon flow at two mooring sites. (a,c) Cross-canyon sections of the up-  
 1327 canyon flow at the locations of the DoMORE sill mooring (Clément et al. 2017) (CTS17-P1) and  
 1328 the BBTRE mooring Thurnherr et al. (2005) (T05). Light grey shading shows the local seafloor  
 1329 depth while the dark grey shading in (a) shows the mean height of the canyon floor above the  
 1330 mean slope, highlighting the significant vertical and cross-canyon constriction introduced by the  
 1331 sill. (b,d) Height-above-bottom profiles of the up-canyon flow at the locations of the two moorings  
 1332 (light grey lines) and shifted a few grid columns over to improve capture the core of the jet (black  
 1333 lines), which is somewhat displaced due to the coarse model bathymetry.



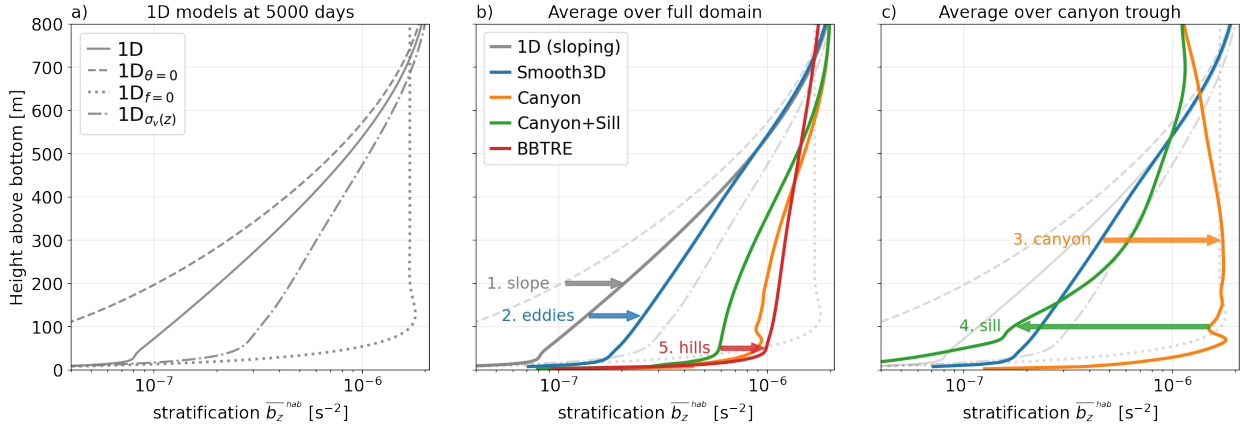
1334 FIG. 6. Comparison between observed and simulated stratification in the BBTRE Canyon region.  
 1335 (a) Height above bottom-averaged profile of stratification for the full simulation domain (solid blue),  
 1336 for the sample-mean of nine co-located CTD casts (dotted red; Ledwell et al. 2000), free-falling  
 1337 HRP-microstructure profiles (dashed red; Polzin et al. 1997), and simulated CTD casts (solid red).  
 1338 The dashed blue line shows the sample-mean of 10 HRP profiles that follow the canyon crest  
 1339 just north of the domain. (b) Observed (solid) and simulated (dashed) density profiles at the  
 1340 nine locations sampled by the BBTRE observational campaign, overlaid on a map of the seafloor-  
 1341 elevation. An additional simulated profile typical of the crest region outside of the canyon is also  
 1342 shown, revealing an apparent sampling bias due to the strategy of measuring weakly-stratified deep  
 1343 depressions along the trough of the canyon in search of the released tracer (Ledwell et al. 2000).



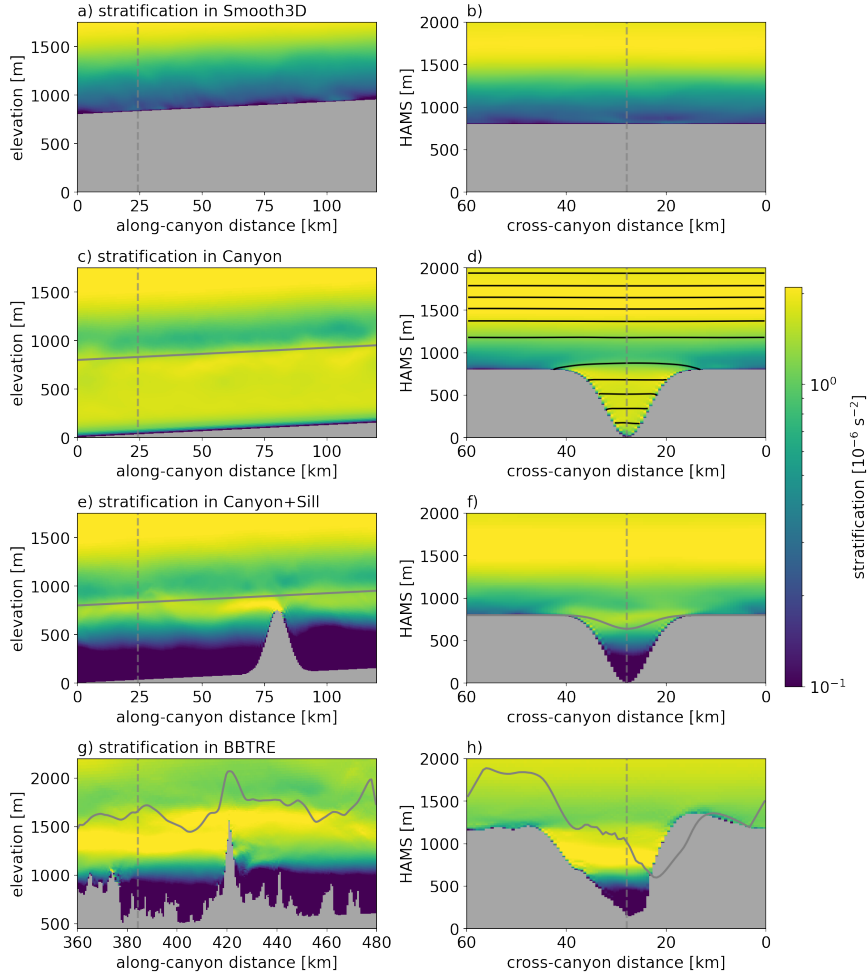
1344 FIG. 7. Instantaneous normalized relative vorticity  $\zeta/f$ , or local Rossby number, in and above  
 1345 the BBTRE Canyon at four different heights above the mean slope, at  $t = 5050$  days.



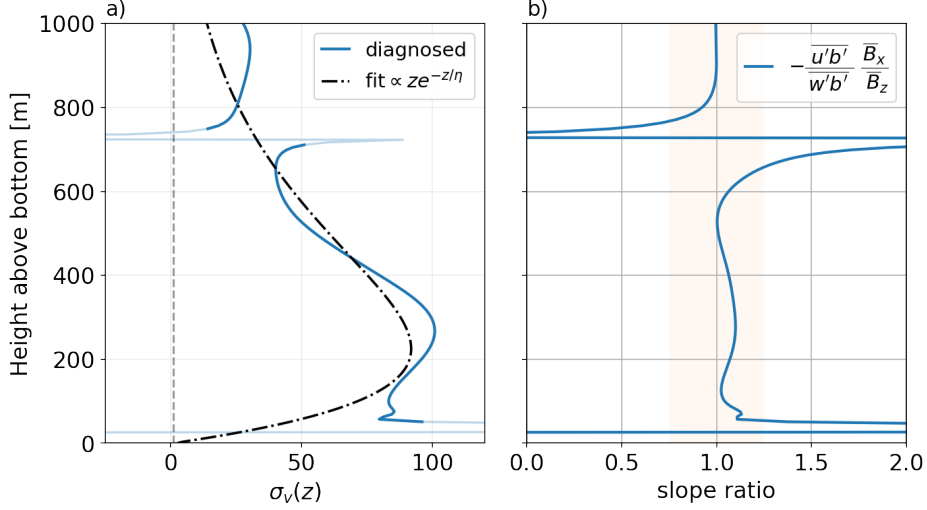
1346 FIG. 8. Generalized integral buoyancy budget in a hierarchy of increasingly complex simulations  
 1347 of mixing-driven flows up a mean slope of angle  $\theta$ : (a) 1D, (b) Smooth3D, (c)  $1D_{\sigma_v(z)}$ , (d) Canyon,  
 1348 (e) Canyon+Sill, (f) BBTRE. Solid lines show terms of the volume-integrated buoyancy budget  
 1349 (eq. 16), averaged over days 5000 to 5200, for a layer bounded by a given Height Above the Mean  
 1350 Slope (HAMS). We interpret the sum of the Mean Flow and Eddy terms as a Residual Flow.  
 1351 The left-hand-side tendencies (LHS) are equal to the remainder of the approximate balance (RHS)  
 1352 between slope-normal turbulent diffusion and the cross-slope residual circulation, which includes  
 1353 both mean and eddy components. We divide (eq. 16) by the factor  $N^2 L_x \sin \theta$  to conveniently  
 1354 express the budget in terms of the quantity of interest, the up-slope volume transport  $\Psi$  with units  
 1355 of  $\text{mSv} \equiv 10^3 \text{ m}^3/\text{s}$ . Dotted lines in (a,c) show 1D steady state solutions and the dashed red line  
 1356 shows the integral constraint (eq. 13); in panels a and b, some of the dotted lines appear missing  
 1357 because they overlap with others. Grey shading shows the HAMS range spanned by the canyon, if  
 1358 present.



1359 FIG. 9. Height above bottom-averaged stratification profiles at  $t = 5000$  days, as a function of  
 1360 model complexity (lines) and domain sub-region (panels b & c). Panel (a) and grey lines in (b,c)  
 1361 show one-dimensional solutions: with the same parameters as the BBTRE simulations (solid);  
 1362 without a mean-slope ( $\theta = 0$ ; dashed), without rotation ( $f = 0$ ; dotted); and with an enhanced  
 1363 along-slope turbulent Prandtl number  $\sigma_v(z)$ , a crude proxy for restratification by submesoscale  
 1364 baroclinic eddies (dash-dotted). Colored lines show a hierarchy of three-dimensional simulations  
 1365 with increasingly complex topographies (see Figure 3c-f). Arrows show how the stratification  
 1366 profiles evolve when processes are added: 1. adding a mean-slope, 2. allowing three-dimensional  
 1367 eddies, 3. introducing a cross-slope canyon, 4. blocking the canyon with a sill, and 5. adding  
 1368 realistic hills (i.e., the BBTRE topography).



1369 FIG. 10. Cross-slope (left) and along-slope (right) sections of the stratification along the trough  
 1370 of a canyon in a hierarchy of numerical simulations (Smooth3D has no canyon, so the section is  
 1371 arbitrary). Solid grey lines in the left column show the approximate elevation of the ridge flanks  
 1372 surrounding the canyon while in the right column they show HAMS of the topographic sill (if  
 1373 present). Dashed grey lines show the locations of the respective sections. Black lines in panel (d)  
 1374 represent equally-spaced buoyancy surfaces.



1375 FIG. 11. a) An idealized  $\sigma_v(z)$  profile (dash-dotted) with vertical scale  $\eta = 225$  m, tuned to  
 1376 the Smooth3D model that resolves submesoscale baroclinic instabilities using equation (A12; solid  
 1377 blue). b) The ratio of the mean isopycnal slope  $s_b = -N^2 \sin \theta / (N^2 \cos \theta + \bar{b}_z)$  to the horizontally-  
 1378 averaged eddy flux slope  $s = \frac{\overline{w'b'}}{u'b'}$ , which is  $\mathcal{O}(1)$  outside of the strongly diabatic and frictional  
 1379 bottom layer. The discontinuity near 750 m is due sign reversals in both the perturbation stratifi-  
 1380 cation and the slope-normal eddy buoyancy flux, which enter in the denominators of expressions  
 1381 for  $\sigma_v$  and  $s^{-1}$ , respectively.